

# GRB 241030A: a bright afterglow challenging forward shock emission

J.-G. Ducoin<sup>1</sup>, C. Pellouin<sup>2</sup>, V. Aivazyan<sup>3,4</sup>, D. Akl<sup>5,6,7</sup>, F. Alvarez<sup>8</sup>, C. Andrade<sup>9</sup>, C. Angulo<sup>8</sup>, S. Antier<sup>5,10</sup>, J.-L. Atteia<sup>11</sup>, S. Basa<sup>12</sup>, R.L. Becerra<sup>8</sup>, Z. Benkhaldoun<sup>13,14</sup>, E. Bissaldi<sup>15,16</sup>, A. Breeveld<sup>17</sup>, E. de Bruin<sup>9</sup>, E. Burns<sup>18</sup>, N.R. Butler<sup>19</sup>, M.W. Coughlin<sup>9</sup>, F. Daigne<sup>20</sup>, T. Dietrich<sup>21,22</sup>, D. Dornic<sup>1</sup>, C. Douzet<sup>10</sup>, T. du Laz<sup>23</sup>, P.-A. Duverne<sup>24</sup>, H.B. Eggenstein<sup>25</sup>, E. Elhosseiny<sup>26</sup>, A. Esamdin<sup>27,28</sup>, P.A. Evans<sup>29</sup>, J. F. Agüí Fernández<sup>30</sup>, M. Ferro<sup>31</sup>, F. Fortin<sup>11</sup>, M. Freeberg<sup>32</sup>, L. García-García<sup>8</sup>, R. Gill<sup>33</sup>, N. Globus<sup>34</sup>, N. Guessoum<sup>35\*</sup>, G.M. Hamed<sup>26</sup>, P. Hello<sup>10</sup>, A. Holzmam Airasca<sup>36,16</sup>, D.F. Hu<sup>37,38</sup>, T. Hussenot-Desenonges<sup>10</sup>, R. Inasaridze<sup>3,4</sup>, A. Iskandar<sup>27,28</sup>, S.Q. Jiang<sup>39,40</sup>, C.C. Jin<sup>39,40,41</sup>, A. Kaeouach<sup>14</sup>, S. Karpov<sup>42</sup>, N. J. Klingler<sup>43,44,45</sup>, A. Klotz<sup>11</sup>, N. Kochiashvili<sup>3</sup>, H. Koehn<sup>21</sup>, R. Kneip<sup>46</sup>, T. Kvernadze<sup>3</sup>, A. Le Calloch<sup>9</sup>, W.H. Lee<sup>8</sup>, A. Letic<sup>47</sup>, Y. F. Liang<sup>37,38\*\*</sup>, C. Limonta<sup>5</sup>, J. Liu<sup>48</sup>, K. Ocelotl. C. López<sup>8</sup>, D. López-Cámara<sup>49</sup>, R.H. Mabrouk<sup>26</sup>, F. Magnani<sup>1</sup>, J. Mao<sup>50,51,52</sup>, M. Mašek<sup>42</sup>, E. Moreno Méndez<sup>53</sup>, B.M. Mihov<sup>54</sup>, M. Molham<sup>26</sup>, K. Noysena<sup>55</sup>, M. Odeh<sup>56</sup>, N. Omodei<sup>57</sup>, H. Peng<sup>48</sup>, M. Pereyra<sup>8</sup>, M. Pillas<sup>58,20\*\*\*</sup>, R. Pillera<sup>16</sup>, T. Pradier<sup>58</sup>, Y. Rajabov<sup>59</sup>, N.A. Rakotondrainibe<sup>12</sup>, B. Schneider<sup>12</sup>, M. Serrau<sup>62</sup>, L. Slavcheva-Mihova<sup>54</sup>, O. Sokoliuk<sup>63,64</sup>, H. Sun<sup>39</sup>, A. Takey<sup>26</sup>, M. Tanasan<sup>55</sup>, K. S. Tinyanont<sup>55</sup>, D. Turpin<sup>65</sup>, A. de Ugarte Postigo<sup>12</sup>, B.T. Wang<sup>66,67</sup>, L.T. Wang<sup>48</sup>, X.F. Wang<sup>48</sup>, Z.M. Wang<sup>41</sup>, A.M. Watson<sup>8</sup>, H.Z. Wu<sup>69</sup>, Q.Y. Wu<sup>39,40</sup>, J.J. Xu<sup>70</sup>, Y.S. Yan<sup>48</sup>, H.N. Yang<sup>39</sup>, W. Yuan<sup>39,40</sup>, and H.S. Zhao<sup>70</sup>

(Affiliations can be found after the references)

Received xx xx, xx; accepted xx xx, xx

## ABSTRACT

**Context.** Gamma-Ray Burst GRB 241030A ( $z = 1.411$ ) exhibited a particularly bright afterglow (similar to the “BOAT”, GRB 221009A), detected across gamma-ray, X-ray, UV, and optical bands. The extensive, multi-wavelength observations of this remarkable event provide a valuable opportunity to advance our understanding of GRB afterglow physics.

**Aims.** We aim to constrain the physical properties of the jet, its microphysics, and the characteristics of the circumburst environment in the context of forward-shock emission

**Methods.** We compiled multi-wavelength observations spanning from a minute to a week after the prompt emission, processing the data through a unified photometry pipeline. Leveraging this comprehensive dataset, we analysed the observations both analytically and using Bayesian inference with two independent models. Our models assume that the afterglow emission arises from the strong forward shock of a laterally structured jet, with possible contributions from synchrotron self-Compton (SSC) scatterings.

**Results.** We find that our models do reproduce the afterglow observations accurately, from the X-rays to the optical, favouring a jet propagating into a constant-density interstellar medium, with a viewing angle within the jet core. However, both analyses – with and without the inclusion of SSC scatterings – require parameter values that are extreme compared to expectations from standard theory. In particular, our results imply extremely energetic jets despite regular prompt energy, leading to a very inefficient prompt emission. Furthermore, the jets are particularly inefficient at accelerating particles, with low  $\epsilon_e$  and  $\epsilon_B$ , leading to significant SSC emission. Finally, our analyses indicate that the jets have large opening angles and propagate in high-density media.

**Conclusions.** If the afterglow is indeed powered by radiation emitted behind a strong forward shock, our results place GRB 241030A within a sub-class of GRBs characterised by extreme kinetic energies, large jet opening angles, and very low prompt emission efficiencies, below  $10^{-3}$ , with strong SSC radiation. These predictions are difficult to reconcile with typical expectations from other GRBs. We therefore suggest that the afterglow of GRB 241030A is not solely powered by forward shock emission, and we discuss other options such as a long-lasting reverse-shock contribution.

**Key words.** (Stars:) Gamma-ray burst: general - (Stars:) Gamma-ray burst: individual: GRB241030A - Radiation mechanisms: non-thermal - Methods: statistical - Techniques: photometric

## 1. Introduction

Gamma-ray bursts (GRBs) are among the most energetic and luminous events occurring in the Universe. They are typically

divided into two broad categories based on the duration of their gamma-ray emission and the hardness of their spectra: long-duration bursts, which last more than two seconds and have ‘soft’ spectra, and short-duration bursts, which last less than two seconds and have ‘hard’ spectra. Long GRBs are generally associated with the core collapse of massive stars, events that are often referred to as ‘collapsars’, while short GRBs are due to the

\* Corresponding author: e-mail: nguessoum@aus.edu

\*\* Corresponding author: e-mail: yfliang@pmo.ac.cn

\*\*\* Corresponding author: e-mail: marion.pillas@iap.fr

merger of a neutron star with another neutron star or a black hole (e.g. [Cano et al. 2017](#); [Abbott et al. 2017](#)). At least one (GRB 170817A) has been associated with gravitational waves ([Abbott et al. 2017](#); [Goldstein & others Fermi GBM Collaboration 2017](#)). In both long and short GRBs, highly relativistic jets are launched from the vicinity of the newly formed compact object. As these jets propagate outward and interact with the surrounding environment, they generate shocks which allow for particle acceleration and give rise to the so-called afterglow emission, from radio to very high energies ([Sari et al. 1998](#); [Sari & Piran 1999](#); [Sari et al. 1999](#); [Piran 2004](#)).

GRB 241030A is a long GRB detected at  $t_0 = 05:48:03$  UT (used in the following as reference  $t_0$ ) on 2024 October 30 ( $T_{90} = 166$  s in 50–300 keV) by the *Fermi* Gamma-ray Burst Monitor (GBM, [de Barra et al. 2024](#)). It was also detected by many other gamma-ray detectors. An observational campaign including several follow-up facilities led to the discovery of the X-ray and optical counterparts and is summarized in Appendix E. Spectroscopic observations provided a redshift measurement of  $z = 1.411$  ([Zheng et al. 2024](#); [Li et al. 2024](#)).

Previous studies have shown a moderate correlation between the afterglow brightness and the isotropic equivalent energy of the prompt gamma-ray emission  $E_{\text{iso}}$  ([Gehrels et al. 2008](#); [Nysewander et al. 2009](#); [Kann et al. 2010, 2011](#)). The case of GRB 241030A offers an opportunity to explore these connections further, to probe the structure and environment of the GRB jet and test the limits of models where only synchrotron emission is accounted for.

In the standard model for GRB afterglows, the GRB jet interacts with the surrounding medium, forming a relativistic forward shock behind which the magnetic field is amplified and electrons are accelerated. This general model, first proposed in the late 1990s, successfully explains the broad-band, smoothly decaying light curves observed in many GRBs ([Mészáros & Rees 1997](#); [Sari et al. 1998](#); [Piran 1999](#)). These accelerated electrons emit synchrotron radiation, whose spectral and temporal evolution depends on microphysical parameters (e.g.  $\epsilon_e$ ,  $\epsilon_B$ , the fractions in the electrons and magnetic field of the total internal energy in the shocked material behind the shock, and  $p$ , the power-law index of the energy distribution of the electrons) and the density profile of the circumburst medium  $n(r)$ , where  $r$  is the radial distance to the source, of the surrounding medium.

Two main types of circumburst media are typically considered: a uniform interstellar medium (ISM) and a stellar wind environment with a density decreasing as  $r^{-2}$ . The ISM model is appropriate for GRBs occurring in constant-density regions, potentially short GRBs associated to mergers which have migrated in their host galaxy away from star-forming regions, while the wind model is consistent with progenitors such as Wolf-Rayet stars that eject strong stellar winds prior to collapse ([Cohen & Piran 1998](#); [Cen et al. 2000](#)). The evolution of the afterglow flux and spectral breaks (for example, the cooling frequency,  $\nu_c$ ) differs significantly between these environments, and distinguishing between them provides insight into the nature of the progenitor and its surroundings.

Furthermore, reverse shocks propagating into the ejecta can produce early-time optical flashes, providing further diagnostics of the outflow properties ([Sari & Piran 1999](#); [Kobayashi 2000](#)). Synchrotron photons can be upscattered to higher energies by the seed electron population, a process known as synchrotron self-Compton (SSC) radiation. This can power the very high energy (VHE) emission detected in some GRB afterglows, such as GRB 190114C ([MAGIC Collaboration et al. 2019a,b](#)) or GRB 221009A ([LHAASO Collaboration 2023](#)). Under cer-

tain conditions (e.g. a very low magnetization), SSC can significantly alter the synchrotron spectrum across all wavelengths and should therefore be included in afterglow models, even in the absence of VHE detection ([Sari & Esin 2001](#); [Nakar et al. 2009](#); [McCarthy & Laskar 2024](#); [Pellouin & Daigne 2024](#); [Hope et al. 2025](#)).

Further research advances extended afterglow modeling to include structured jets, energy injection, and magnetization. In structured jet models, the energy per solid angle varies with the angle from the jet axis (see early works by e.g. [Mészáros et al. 1998](#); [Panaitescu & Kumar 2003](#)), which can account for the observed diversity in afterglow behavior and explain events observed off-axis, such as GRB 170817A ([Lamb & Kobayashi 2017](#); [Troja et al. 2017](#); [Hallinan et al. 2017](#); [Liang et al. 2018](#); [Ghirlanda et al. 2018](#); [Granot et al. 2018](#)).

In the case of GRB 241030A, interest in following this burst quickly emerged because its afterglow appeared very bright in UV/optical in the initial observations. Its well-sampled afterglow across the X-ray, optical and infrared bands provides an excellent opportunity to test afterglow models. The temporal and spectral evolution of the emission may help discriminate between an ISM or wind-like environment, constrain the jet geometry, and evaluate the role of energy injection or jet structure. Yet, [Wang et al. \(2025a\)](#) have investigated the prompt thermal X-ray emission component and origins of the very early UVOT clear and  $U$  band emission. Using early *Swift*-XRT and *Swift*-UVOT observations of GRB 241030A, [Wang et al. \(2025a\)](#) found strong optical variability that traces the gamma-ray activity, possibly from internal shocks. A thermal component, likely photospheric, was found with a temperature of a few keV and an inferred Lorentz factor between 20 and 80. A sharp rise in the  $U$ -band suggested the onset of external shock emission. Thus, we aim to complement these investigations by looking at the multi-wavelength afterglow observation from a minute to 9.5 days after the prompt emission. Additional studies of the prompt emission have been presented in [Wang et al. \(2025b\)](#); [Varun et al. \(2025\)](#), which analyse the gamma-ray and early X-ray emission of GRB 241030A.

In Section 2, we present the multi-wavelength (gamma-ray to optical) afterglow observations of GRB 241030A. In Section 3, we determine the line-of-sight extinction and leverage our optical follow-up observations to search for the host galaxy. Section 4 is dedicated to the multi-wavelength study of the afterglow of GRB 241030A, using an analytical approach and Bayesian inference with two different models. Finally, in Section 5, we discuss our findings and conclude this work in Section 6.

## 2. Multi-wavelength observations of GRB 241030A

The gamma-ray & X-ray observations used in the following analysis are presented in Appendix F, Table F.1 and shown in Fig. 1. The UV/optical observations used in the analysis are presented in Appendix F, Tables F.2,F.3,F.4,F.5,F.6 and are also shown in Fig. 1. The optical data points are also accessible in the [Skyportal page of the event](#).

### 2.1. Prompt: $E_{\text{iso}}$ computation

We calculated the total isotropic-equivalent energy released in gamma-rays using measurements from both *Fermi*-GBM and *Konus-Wind*. [Ridnaia et al. \(2024\)](#) report the *Konus-Wind* measurement of  $E_{\text{iso}} = (2.84^{+1.04}_{-0.68}) \times 10^{53}$  erg. For *Fermi*-GBM we utilize the initially reported time-integrated spectral results from the *Fermi*-GBM team ([de Barra et al. 2024](#)). This corresponds

to a fluence of  $(6.2 \pm 0.1) \times 10^{-5}$  erg · cm<sup>-2</sup>, from a best-fit Band function with a peak energy  $E_{\text{peak}} = (130 \pm 10)$  keV, low-energy index  $\alpha = -1.35 \pm 0.02$ , and high-energy index  $\beta = -2.3 \pm 0.1$ . Accounting for the cosmological  $k$ -correction (Bloom et al. 2001), we calculate  $E_{\text{iso}} = (4.0 \pm 0.1) \times 10^{53}$  erg. We also extract time-resolved spectra from the Fermi-GBM data, and by combining the fluxes from the best-fit Band function in each interval, we yield a consistent  $E_{\text{iso}} = (4.4 \pm 0.2) \times 10^{53}$  erg. A similar order of magnitude  $E_{\text{iso}} = (3.3 \pm 0.1) \times 10^{53}$  erg was also reported by Varun et al. (2025), employing smoothly broken powerlaw models with high-energy cutoff.

## 2.2. Early afterglow with Swift

After slewing to the burst, *Swift*-UVOT started collecting data at approximately  $t_0 + 80$  s, while the GRB was still in its prompt phase ( $T_{90} \sim 200$  s). In the white band, the emission appears to rise until around  $t_0 + 120$  s, at which point it peaks (with an AB mag of about 15.6), then fades shortly after. At about  $t_0 + 200$  s, the emission starts to rise again. In the  $u$  band, the emission rises again until about  $t_0 + 400$  s, peaking at 13.6 mag (AB), after which point it begins to fade again following a power-law decay. Thus, we refer to times before  $t_0 + 400$  s as the prompt emission, and times after  $t_0 + 400$  s as the afterglow.

In X-rays, during the prompt emission phase a very bright flare can be seen from about 80 s to 430 s post-trigger. The flare exhibits substantial variability, but the average brightness peaks at around 180 s. After 430 s, the X-ray emission begins to follow a power-law decay. A joint analysis of the X-ray and gamma-ray (*Swift*-BAT) data by Wang et al. (2025a) found the presence of a thermal component with a temperature of a few keV during the flare period, which the authors interpreted as the photosphere radiation. They also attribute the  $u$ -band peak to the onset of the external shock emission.

## 2.3. Afterglow: Gamma-ray data

The burst was detected by the *Fermi*-LAT (Atwood et al. 2009) in the 100 MeV–100 GeV range (Pillera et al. 2024), occurring 19° from the LAT boresight at the time of the GBM trigger ( $t_0$ ) and remaining in the Field of View (FoV) for  $\sim 800$ s. In this time interval we performed a standard LAT data analysis, following the procedure described in Ajello et al. (2019), and implemented with the “Multi-Mission Maximum Likelihood” (ThreeML, Vianello et al. 2015). We detected 9 high-energy photons with more than 90% probability of association with the GRB. The highest-energy photon detected was a 2 GeV event at  $t_0 + 470$  s. Therefore, the analysis was restricted to the 100 MeV–10 GeV range. The *Fermi*-LAT events were binned, with each bin containing at least three significant photons and a detection with at least  $3\sigma$  significance. For each time interval, using the *Fermi*-LATlike plugin, we conducted an unbinned maximum likelihood fit of the energy spectrum using a simple power-law (PL) model,  $F(E) = F_0 \times \left(\frac{E}{E_0}\right)^{-\gamma}$ , where the flux normalization  $F_0$  and the photon index  $\gamma$  were treated as free parameters. The resulting light curve is shown in Fig. 1 (black dots) and the data is provided in Table F.1. The GRB position re-enters the LAT FoV from about 5 ks and until about 13 ks. Standard analysis resulted in no detection and we computed upper limits. We searched for an extended emission covering the whole afterglow period observed by the other instruments (until 700 ks), but no significant high-energy emission was detected. More details are available in Appendix C.

## 2.4. Afterglow: X-ray data

We analysed X-ray data from *Swift*-XRT, *EP*-WXT, and *EP*-FXT. First, the XRT light curve (0.3–10 keV) of GRB 241030A was acquired from the UK Swift Science Data Center and extracted from the burst analyser<sup>1</sup> (Evans et al. 2007, 2009). We performed a re-binning of the XRT light curve by dividing the observations into fifteen time windows in the same way as in Kann et al. (2023). For each time window we computed the mean value and standard deviation to produce single data points. The light curve is presented in Fig. 1 and the data is provided in Table F.1.

Secondly, we analysed observations from *EP*-WXT (Cheng et al. 2025) from 2715 seconds after  $t_0$  with an exposure of approximately 1.2 ks. The light curve exhibited no significant variability throughout the observation. The spectrum was fitted in XSPEC by an absorbed power law model *tbabs*\**tbabs* \**powerlaw* (Arnaud et al. 1999), where a fixed redshift of 1.411 was used, and the column density was fixed at the Galactic value of  $N_{\text{H}}^{\text{Gal}} = 1.79 \times 10^{21}$  cm<sup>-2</sup>. It should be noted that the flux derived from WXT corresponds to the 0.5–4 keV energy band. Subsequently, we performed three follow-up observations with the FXT (Chen et al. 2021) in the 0.5–10 keV band. For the spectral fitting, we applied the same model used for the WXT data. Due to the low photon statistics in the last FXT observation, we combined data from the final two observational epochs to perform a joint fit. We provide the results in Table F.1 and include the light curve in Fig. 1.

## 2.5. Afterglow: UV/Optical data

The *Swift*-UVOT data was analysed using the standard UVOT tools included with HEASoft (v6.34). Most of the data from the first orbit (i.e., data collected before 2024-10-30 06:03 UTC) were taken with UVOT operating in Event Mode (in which each event is time-tagged with a resolution of 11 ms), so we used *uvotevt1c* to create background-subtracted light curves from the event data, using a time binning of 20 seconds. For the rest of the data, collected in Imaging Mode, we calculated the magnitudes using the standard tool *uvotsource* for all filters (white,  $v$ ,  $b$ ,  $u$ , *uvw1*, *uvm2*, and *uvw2*). Due to the source’s high brightness during the first orbit, we used an  $r = 15''$  source extraction radius (i.e., aperture), and an  $r = 6''$  extraction radius for all subsequent data. We used two source-free regions ( $r = 20''$  and  $r = 45''$ ) within 1.5' of the burst position for the background regions (required input by *uvotsource* and *uvotevt1c* for background subtraction).

Besides, we processed in a coherent approach all the optical images from GRANDMA, KNC and COLIBRÍ together with images from TRT-SRO  $R$  band presented by Wang et al. (2025a). All images in clear, *GAIA* –  $RP$ ,  $R$ ,  $V$ ,  $I$ ,  $B$ ,  $g'$ ,  $r'$ ,  $i'$ , and  $z'$  underwent telescope-specific pre-processing, including bias, dark subtraction, and flat-fielding. For some images, co-addition was performed using the SWarp software (Bertin 2010) to enhance signal-to-noise ratio, and astrometric solutions were acquired using Astrometry.net (Lang et al. 2010). All data have been reduced by a single data processing pipeline, STDPIPE<sup>2</sup> (Karpov 2021, 2025), a python package that uses pre-configured scripts for image analysis. Specifically, we used the online implementation of the package called STDweb<sup>3</sup>. For photometric calibration, the catalogs were chosen based on the filters used in the images. The images acquired with sloan filters were calibrated using the Pan-

<sup>1</sup> [https://www.swift.ac.uk/burst\\_analyser/](https://www.swift.ac.uk/burst_analyser/)

<sup>2</sup> <https://gitlab.in2p3.fr/icare/stdpipe>

<sup>3</sup> available at <http://stdweb.favor2.info/>

STARRS DR1 catalog (Chambers et al. 2016). Images observed with Johnson-Cousins filters were calibrated using the Gaia DR3 Syntphot catalog (Gaia Collaboration et al. 2023), which offers synthetic photometry from low-resolution (XP) spectra of stars observed by Gaia. Lastly, images observed without a filter cover a broad wavelength range, making standard calibration difficult. Hence, we used the  $G$ -band from the Gaia eDR3 catalog (Gaia Collaboration et al. 2023) to handle these images. For the analysis below, we corrected UV/Optical observation for Galactic extinction using the approach of Schlafly & Finkbeiner (2011).

### 3. Host galaxy extinction and characterisation

#### 3.1. Line-of-sight extinction

To estimate the line-of-sight host galaxy dust extinction, we created an X-ray-to-optical spectral energy distribution (SED) with *Swift*-XRT and optical data in the  $u, b$  bands from *Swift*-UVOT;  $B, R, I$  from TRT and  $r$  from COLIBRÍ at a common time of  $t - t_0 \sim 3$  h after the burst trigger. The optical data was interpolated to this mid-time and the time-sliced X-ray spectrum was acquired from the automated data products provided by the public *Swift*-XRT repository (Evans et al. 2007).

We performed the SED fit by following a standard routine using the typical extinction curves of the Milky Way (MW) and the Large (LMC) and Small Magellanic Clouds (SMC) prescribed in Pei (1992). The intrinsic X-ray-to-optical spectrum was modeled with a single or broken power law according to the afterglow theory (Sari et al. 1998). According to the standard afterglow model, in the slow cooling regime the spectral index above the cooling frequency is expected to be steeper by 0.5 than that below it (see Section 4.1). We therefore fixed the X-ray slope to be 0.5 larger than the optical one, i.e.  $\Delta\beta = \beta_X - \beta_o = 0.5$ . By fixing the redshift and the Galactic foreground absorption of  $N_{\text{H}}^{\text{Gal}} = 1.79 \times 10^{21} \text{ cm}^{-2}$  (Collaboration et al. 2016; Willingale et al. 2013), the best fit is given by a broken power law with a MW extinction curve (Fig. 2). The best fit parameters are  $\beta_X = \beta_o + 0.5 = 1.045 \pm 0.062$  ( $E_{\text{break}} = 0.022 \pm 0.016$  keV), and  $E(B - V) < 0.195$  mag at  $3\text{-}\sigma$  confidence level with  $\chi^2/\text{d.o.f} = 19.057/17$ . The fit with the LMC extinction curve also gives a reasonable fit ( $\chi^2/\text{d.o.f} = 20,077/17$ ) yielding  $\beta_X = \beta_o + 0.5 = 1.045 \pm 0.059$  ( $E_{\text{break}} = 0.043 \pm 0.029$  keV), and  $E(B - V) < 0.102$  mag. This is compatible with standard values observed for long GRBs at this redshift (e.g. Schady et al. 2012; Rakotondrainibe et al. 2024). However, with the lack of NIR data, this amount of extinction might be underestimated. The process of determining optical extinction is more complex without NIR data points, which are less affected by dust extinction than the UV and blue bands. In addition, they can play a role as an anchor for the determination of the intrinsic spectral shape of the afterglow. As a further test, we performed the SED fit at two different epochs, i.e.  $t - t_0 \sim 0.19$  h, using  $uvw2, uvm2, uvw1, u, b, v$ -bands and  $\sim 22$  h, with  $uvw2, uvm2, uvw1, u, b, v, g, r, i$ , in the same manner as previously. The resulting values of the extinction remained consistent with this limit of  $E(B - V) < 0.195$  mag. In light of this analysis, we used in the following an  $E(B - V) = 0.1$  mag to correct our observations from the host extinction.

#### 3.2. Host galaxy study

We first used the long-term follow-up observation from COLIBRÍ to stack all the images acquired from June 6 to June 10, 2025 (from 219 to 223 days post-trigger) with a total of about 21.43 hours of images. This allowed us to get a deep image of the field

at a time when the afterglow contribution was low and to search for a potential host galaxy. In this image, we identified an extended object near the afterglow position at RA = 343.1419, Dec = 80.4496 (deg), which we initially considered as a putative host galaxy of the GRB. Thus, we requested observation with CFHT-MegaCam in  $r$  and  $i$  bands and with GTC-HiPERCAM in  $u, g, r, i$ , and  $z$  bands. The putative host was well detected in these observations, but these precise measurements of the galaxy allowed us to measure an offset of  $1.74 \pm 0.18$  arcsec with the afterglow position. Assuming the Planck Collaboration et al. (2020)'s cosmological parameters, at GRB 241030A's redshift  $z = 1.411$ , this would represent a physical offset of  $15.10 \pm 1.56$  kpc. This value being significantly larger than typical long GRB offsets (e.g. Blanchard et al. 2016), we discarded this galaxy as candidate host. To confirm this rejection, we performed the SED fitting of this galaxy using CIGALE<sup>4</sup> (Code Investigating GALaxy Emission; Boquien et al. 2019), adopting a parameter space similar to Corre et al. (2018), keeping the redshift as free parameter in the range [0.4, 1.5]. We hence obtained a photometric redshift of  $z = 0.50^{+0.19}_{-0.10}$ . This redshift is compatible with absorption lines detected at lower redshift in the afterglow spectrum (Zheng et al. 2024). We hence conclude it is not the host of GRB 241030A but a foreground galaxy. No other sources are detected in CFHT and GTC images near the afterglow position down to magnitudes  $i < 25.62$  and  $r < 25.82$ . The non-detection of a host at  $z = 1.411$  is consistent with previous long GRBs at similar redshifts, for which hosts were found to be faint ( $r > 25\text{--}26$  mag) or undetected even in deep observations (e.g. Cenko et al. 2008; Greiner et al. 2015; Perley et al. 2016b,a). Our limiting magnitudes thus do not exclude the presence of a typical faint GRB host, especially if moderately dust-obscured.

### 4. Multi-band afterglow modeling

#### 4.1. Empirical Light curve analysis

We start by analysing the afterglow of GRB 241030A empirically, that is using a power-law function of the form  $F_\nu \propto t^{-\alpha} \nu^{-\beta}$  to characterise its temporal and spectral evolution. We obtain a temporal decay slope  $\alpha = 1.23 \pm 0.01$  and a spectral slope  $\beta = 0.70 \pm 0.01$  across all X-ray and optical filter bands and before  $\sim 10^4$  s, when the X-ray light curve steepens slightly. These values are typical for long GRB afterglows (e.g. Evans et al. 2009; Del Vecchio et al. 2016) and in agreement with standard synchrotron emission from the region behind the forward shock (Sari et al. 1998).

The long-term GRB afterglow synchrotron emission is usually expected to be in the slow-cooling regime for standard jet and environment parameters (e.g. Granot & Sari 2002). Assuming that all radiation is emitted behind the forward shock and that all measured bands fall between the minimum injection frequency  $\nu_m$  and the cooling frequency  $\nu_c$ , we can use the analytical relations between  $p$ , the electron energy distribution index,  $\alpha$ , and  $\beta$  (Sari et al. 1998; Panaitescu & Kumar 2000) to estimate  $p$  from the values of  $\alpha$ . A homogeneous medium gives  $\alpha = \frac{3}{4}(p - 1)$ , which results in  $p = 2.64 \pm 0.01$ , while a wind-like medium gives  $\alpha = \frac{3p-1}{4}$ , corresponding to  $p = 1.97 \pm 0.01$ . For the spectral slope,  $\beta = \frac{p-1}{2}$  which yields  $p = 2.40 \pm 0.01$ . There is a discrepancy between the values of  $p$  obtained from the spectral and the temporal analyses, which hints at a potentially more complex radiation scenario that includes other effects such as contributions from the lateral structure of the jet, or modifications to the

<sup>4</sup> <http://cigale.lam.fr>

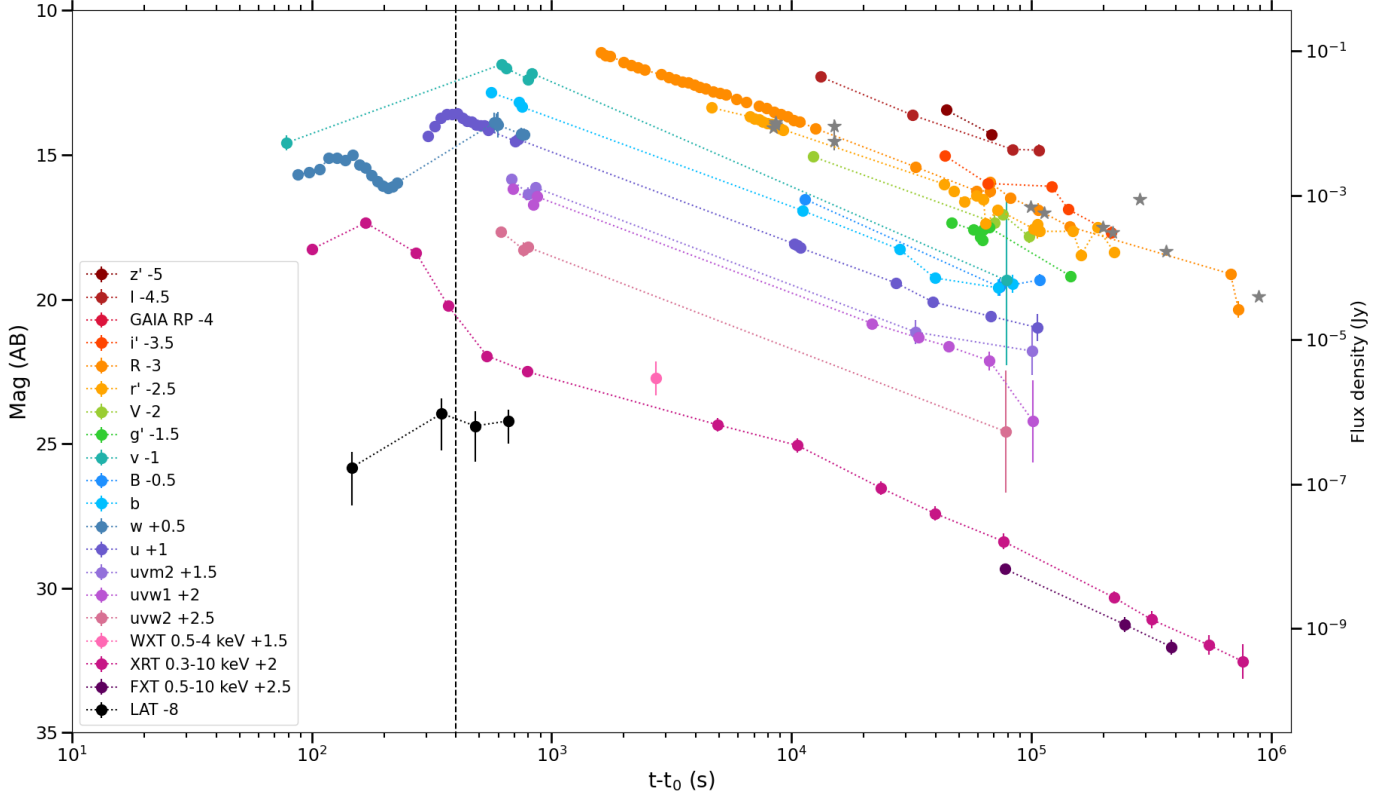


**Fig. 1.** Light curves of GRB 241030A, corrected for Galactic and host extinction. Observations after the vertical dashed line (shown at 400 s post T0) were used for the afterglow analysis in Section 4. Grey stars are GRB 221009A  $r'$  band magnitude from Kann et al. (2023), adjusted to redshift 1.411 with  $k$ -correction,  $-2.5$  magnitude for comparison with the GRB 241030A  $r'$  light curve (see Section 4.3).

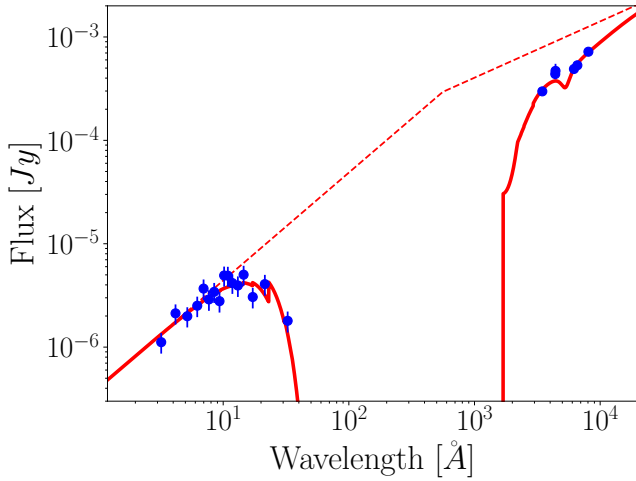


**Fig. 2.** SED of the afterglow of GRB 241030A at  $t - t_0 \sim 3$  h. The dashed line corresponds to the intrinsic broken power law model. The solid line represents the best fit to the data, and includes the absorption in the X-ray band.

emitted spectrum by SSC (synchrotron self-Compton) scatterings (see Section 4.4). The values of  $p$  are substantially inconsistent in the case of a wind-like medium, while the value of  $p \sim 2.5$  resulting from a homogeneous medium (Sari et al. 1998), is a reasonable index for particle acceleration in shocks. In this scenario, the slight steepening of the X-ray light curve after  $\sim 10^4$  s can be interpreted by the passage of  $v_c$  in the X-ray band. Based

on this first analysis, we now investigate the scenario in which the observed afterglow is dominated by synchrotron radiation from a forward shock propagating in a homogeneous medium.

#### 4.2. Bayesian methods and data analysis

To study the physical properties of the jet, we fit the observed light curve data with two physical GRB afterglow models. Specifically, we rely on AFTERGLOWPY (Ryan et al. 2020) and on the afterglow model from Pellouin & Daigne (2024), hereafter referred to as PD24. Both of these models assume that the emission arises when a laterally-structured relativistic jet interacts with the cool, constant-density interstellar medium and treat the forward shock dynamics and radiation emission in a semi-analytical fashion. The AFTERGLOWPY framework includes a treatment of the late-time lateral expansion of the jet, thus providing a more accurate calculation of the jet deceleration than PD24 in the trans-relativistic and Newtonian regimes. On the other hand, PD24 includes a treatment of synchrotron self-Compton (SSC) scattering in both Thomson and Klein-Nishina regimes, which can decrease the synchrotron emissivity and modify the synchrotron spectral shape (see Pellouin & Daigne 2024; Nakar et al. 2009; Aguilar-Ruiz et al. 2025). The initial coasting phase is also included in PD24.

In both analyses, we rely on the gaussian jet model where the initial isotropic-equivalent kinetic energy of the blastwave at any

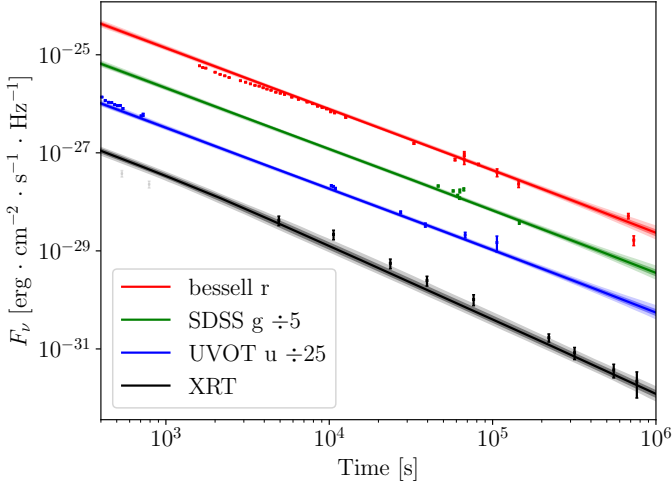


**Fig. 3.** Light curve fits for selected filters from the NMMA inference with the AFTERGLOWPY gaussian jet model. Observed data and their uncertainties are shown as error bars; the solid lines indicate the median value of the posterior sample at each time. The shaded contours correspond to the 68% and 95% quantiles of the posterior distribution. The two transparent XRT data points before  $10^3$  s were not included in the fit.

angle  $\theta$  follows the distribution

$$E(\theta) = E_0 \exp\left(-\frac{\theta^2}{2\theta_c^2}\right), \quad (1)$$

with  $\theta$  the polar coordinate angle measured from the jet axis and  $\theta_c$  the core angle, a free parameter of both models, and  $E_0$  the energy measured at the jet axis ( $\theta = 0$ ). For the analysis with AFTERGLOWPY we sample the posterior distribution of the light curve using the NMMA (Nuclear-physics and Multi-Messenger Astrophysics) Bayesian inference framework (Pang et al. 2023). The posterior on the model parameters  $\vec{\theta}$  is determined in NMMA by invoking the likelihood function

$$\ln \mathcal{L}(\vec{\theta}|d) = - \sum_{t_j} \left( \frac{1}{2} \frac{(m(t_j) - m^*(t_j, \vec{\theta}))^2}{\sigma(t_j)^2 + \sigma_{\text{sys}}^2} + \ln(2\pi(\sigma(t_j)^2 + \sigma_{\text{sys}}^2)) \right). \quad (2)$$

Here,  $m(t_j)$  are the observed magnitudes with corresponding measurement uncertainties  $\sigma(t_j)^2$ , and  $m^*(t_j, \vec{\theta})$  is the corresponding prediction of the AFTERGLOWPY gaussian jet model for a given set of parameters  $\vec{\theta}$ . The parameter  $\sigma_{\text{sys}}$  accounts for possible systematic uncertainties caused by simplifying assumptions in the model. Since the latter is hard to assess a priori, we introduce  $\sigma_{\text{sys}}$  as a sampling parameter and assess the need for a systematic error on-the-fly during the inference. This method has been suggested in Jhavar et al. (2025) and is implemented in NMMA. Specifically, the prior for  $\sigma_{\text{sys}}$  is uniform between 0.01 and 2 mag.

For the analysis with PD24, we use a similar gaussian jet model and the likelihood function is expressed as in Eq. 2, without the introduction of the free parameter  $\sigma_{\text{sys}}$ . Instead, we introduce a systematic contribution to the errors in the data such that each observation has at least a 0.2 mag error. As shown by the fit

**Table 1.** Parameters and priors used for the Bayesian analyses using the physical afterglow models. The two last columns contain the 95% credible posterior interval for each particular parameter. The bar indicates that the parameter is not used by that model.

Parameters	Symbol	Prior	AFTERGLOWPY	
			NMMA/	PD24
cos inclination [rad]	$\cos(\iota)$	[0, 1]	$0.97^{+0.02}_{-0.03}$	$0.99^{+0.01}_{-0.00}$
log isotropic kinetic energy [erg]	$\log_{10}(E_0)$	[50, 60]	$56.9^{+1.6}_{-1.1}$	$56.2^{+0.7}_{-0.7}$
jet core angle [deg]	$\theta_c$	[0.056, 10]	$8.6^{+1.1}_{-2.3}$	$9.7^{+0.1}_{-1.7}$
wing factor	$\alpha_w$	[0.2, 3.5]	$2.72^{+0.72}_{-1.02}$	-
log interstellar medium density [ $\text{cm}^{-3}$ ]	$\log_{10}(n_{\text{ism}})$	[-6, 4]	$2.9^{+1.0}_{-4.6}$	$2.5^{+0.7}_{-0.7}$
electron spectrum power index	$p$	[2, 3]	$2.62^{+0.05}_{-0.04}$	$2.57^{+0.16}_{-0.06}$
log electron energy fraction	$\log_{10}(\epsilon_e)$	[-4, 0]	$-2.25^{+0.67}_{-1.27}$	$-3.32^{+0.67}_{-0.66}$
log magnetic energy fraction	$\log_{10}(\epsilon_B)$	[-8, 0]	$-6.98^{+2.64}_{-0.90}$	$-4.17^{+0.76}_{-0.72}$
log accelerated electrons fraction	$\log_{10}(\zeta)$	[-3, 0]	-	$-0.70^{+0.67}_{-0.65}$
initial Lorentz factor	$\Gamma_0$	[50, 500]	-	$432^{+65}_{-137}$
systematic uncertainty [mag]	$\sigma_{\text{sys}}$	[0.01, 2]	$0.21^{+0.03}_{-0.03}$	-

with NMMA/AFTERGLOWPY (see Fig. D.1), this is a reasonable assumption, since  $\sigma_{\text{sys}}$  converges to values around that error.

The priors for the analyses are listed in Table 1. For the common parameters in the AFTERGLOWPY and PD24 models, the priors are kept identical. As discussed above,  $\sigma_{\text{sys}}$  is only introduced in NMMA/AFTERGLOWPY, as well as the wing factor  $\alpha_w$  which determines the angular extent of the lateral structure. PD24 includes two additional free parameters:  $\zeta$ , describing the fraction of electrons which are accelerated behind the shock; and  $\Gamma_0$ , the initial Lorentz factor of the jet until the deceleration radius (during the coasting phase). Note that  $\Gamma_0$  is kept uniform and does not have an angular profile.

We only fit data points measured more than 400 s post-trigger time, to avoid any influence of the prompt emission on the analysis and focus on the external shock as suggested by Wang et al. (2025a). The upper limits were not included in the fit, as none of them was expected to provide significant constraints, particularly given the large size of the dataset. Luminosity distance and redshift are fixed to  $d_L = 10.3$  Gpc and  $z = 1.411$ , respectively. Moreover, we exclude data points in the UV bandpasses that include wavelengths below the Lyman- $\alpha$  break for this particular redshift, i.e. below 2190 Å. Specifically, these are the *Swift*-UVOT *uvw1*, *uvw2*, *uvm2* and white filters.

In the analyses with NMMA/AFTERGLOWPY, we exclude the LAT data points and the early XRT data before  $10^3$  s. If we include the early XRT data in the NMMA/AFTERGLOWPY analyses, it causes a bimodality in the inferred electron power law index  $p$ . We suggest this behavior is due to the slight change of slope in the XRT data from early to late times, leading the AFTERGLOWPY model to overestimate the flux at early times when fitting to the slope of the late-time X-ray data. To offset this, the sampler finds a second mode with higher  $p$  that captures the early part of the light curve better. However, this mode predicts even more extreme values for the jet energy and fraction of energy accelerating electrons  $\epsilon_e$  as well as a larger inclination, and fits less well to the majority of the XRT data. Additionally, this set of solutions leads to coasting phase durations of about  $10^3$  s, which are not accounted for by the model. Hence, we conclude that this second mode is unphysical and exclude the early XRT data in the NMMA/AFTERGLOWPY analyses to avoid impact on our conclusions. Observations between 400 and 1000 s are included in the fit with PD24.

#### 4.3. Results from NMMA/afterglowpy – Synchrotron

The best-fit light curves for the AFTERGLOWPY analysis are shown in Fig. 3. In Appendix D, we show the posterior distribution of the fits in Fig. D.1 (light blue contours). We also show the posterior for a fit with PD24 that does not include SSC (pink contours), giving a very good consistency between the two models. In this section, we thus discuss only the results from NMMA/AFTERGLOWPY. Overall, the model manages to fit the light curve within the expected systematic modeling uncertainties. The fit slightly underestimates the early UV data, which could originate from an additional radiating region (e.g. a reverse shock, as discussed in Wang et al. 2025a). The resulting posteriors (Appendix D, light blue contours) demonstrate that the NMMA/AFTERGLOWPY sampling appropriately explores the parameter space and retrieves the degeneracies usually observed in afterglow modeling.

This analysis favors solutions corresponding to the analytical description of Section 4.1: the emission is powered by synchrotron emission of slow-cooling electrons between  $\nu_m$  and  $\nu_c$  in all bands until  $\sim 10^4$  s, where  $\nu_c$  crosses the X-ray band, which is a standard case of afterglow observations.

What deviates from standard afterglow theory is the values of some of the parameters inferred by the Bayesian fit. The analysis points to an energetic jet with  $\log_{10}(E_0) = 56.9^{+1.6}_{-1.1}$ . (The intervals throughout this article mark the 95% credibility limit.) The typical afterglow kinetic jet energy  $E_0$  is usually limited to  $\lesssim 10^{56}$  erg (Lloyd-Ronning & Zhang 2004; Aksulu et al. 2022), but the high energy we find for this GRB afterglow is in agreement with Wang et al. (2025a), as their analysis suggests  $\log_{10}(E_0) = 55.83^{+0.18}_{-0.18}$ . These high energy values are partially correlated to the low value for  $\epsilon_e < 10^{-2}$  that our anal-

ysis also infers. The fraction  $\epsilon_B$  is also found to be very low:  $\epsilon_B \sim 10^{-7}$ . As a secondary check, we thus reran the analyses with  $\epsilon_e$  fixed to a more canonical value of 0.1. However, while these analyses indeed recover more moderate values for the energy at around  $10^{55.5}$  erg, they deliver worse fits for most bands and increase the overall  $\chi^2$ -residuals notably. Fixing  $\epsilon_e$  in the NMMA/AFTERGLOWPY analyses also causes  $n_{\text{ism}}$  to rail against the upper prior bound of  $10^4$  cm $^{-3}$  while the Bayesian evidence drops by a factor of 900 compared to the case where  $\epsilon_e$  is left free.

We investigated the energy budget of GRB 241030A by computing the kinetic energy corrected from the beaming, assuming a gaussian jet structure and using the results from our (most energetic) afterglowpy run (see Appendix D). We obtain

$$E_{\text{kin}} = 2\pi \int_0^{\theta_w} d\theta \sin(\theta) \frac{E_0}{4\pi} \exp\left(-\frac{\theta^2}{2\theta_c^2}\right) \approx 8.7 \times 10^{54} \text{ erg} . \quad (3)$$

In comparison, for the very bright GRB 221009A the estimates are between  $E_0 = 10^{54}$  and  $10^{55}$  erg, but with a much narrower jet core, leading to more typical values of  $E_{\text{kin}}$  (e.g. O’Connor et al. 2023; Gill & Granot 2023). Under this scenario, this afterglow would be almost two orders of magnitude more energetic than GRB 221009A, making it one of the most energetic GRB afterglows so far. What stands out directly from our observations is that the afterglow of GRB 241030A is indeed very bright. We illustrate this by plotting the GRB 221009A  $r'$  band light curve, placed at  $z = 1.411$ , against our GRB 241030A light curve in Fig. 1 (gray stars), for inter-comparison, which shows similar luminosities. However, the model parameters that we obtain here are much more extreme: given the GRB prompt duration of 300 s, accounting for breakout from the star, the jet power needed to accumulate this much energy corresponds to a jet luminosity of  $L_j \sim 5 \times 10^{53}$  erg s $^{-1}$ , which may be difficult to explain in the collapsar scenario.

It is also noteworthy that, contrary to GRB 221009A, such a large kinetic energy is much larger than the prompt emission energy  $E_{\text{iso}} = 4 \times 10^{53}$  erg as determined in Section 2.1, and our values for  $E_0$  would imply a prompt emission efficiency of  $\eta \lesssim 10^{-3}$ , where we define  $\eta = E_{\text{iso}}/E_{\text{tot,iso}} = 1/(1 + E_0/E_{\text{iso}})$ , where we assumed that the Lorentz factor of the ejected material along the line of sight is identical to the prompt Lorentz factor. Typical expected values for  $\eta$  are within 0.01–0.9 (Beniamini et al. 2016; Racusin et al. 2011), though we should note that a new sample of low-efficiency long GRBs recently emerged due to more sensitive transient detection facilities (Sarin et al. 2022; Ye et al. 2024; Li et al. 2025). We also performed a NMMA/AFTERGLOWPY analysis where we set a lower limit on  $\eta$  of 0.01, effectively constraining  $\log_{10}(E_0) \leq 54.9$ , however, this delivers a notably worse fit compared to a free  $\log_{10}(E_0)$ . Specifically, we find a Bayes factor of 300,000 in favor of the inference with a uniform prior  $\log_{10}(E_0) \sim \mathcal{U}(50, 60)$  against the inference with a uniform prior  $\eta \sim \mathcal{U}(0.01, 1)$ . Additionally, we performed a fit with the AFTERGLOWPY top-hat jet model, however this does not result in lower energy values either and is decisively disfavored with a Bayes factor of 230 compared to the gaussian jet model. Similar results are obtained with the top-hat model with PD24. Finally, we also conducted a fit for a top-hat jet propagating in a wind environment with the PD24 model. This analysis did not perform better than for the case with a constant external density. We thus conclude that, if the afterglow is powered by synchrotron radiation of electrons accelerated behind a forward shock at the measured redshift  $z = 1.411$ , the high jet energy coupled to a

weak radiative efficiency (low  $\epsilon_e$ ,  $\epsilon_B$ ) offers the best explanation for the brightness observed in the afterglow of GRB 241030A.

Moreover, our analyses find a relatively large opening angle for the core of the jet  $\theta_c = 8.6_{-2.3}^{+1.1}^\circ$ , which is impacted by our upper prior bound of  $10^\circ$ . Such opening angles are higher than for typical GRB jets, but still consistent with jet ejection theory. Goldstein et al. (2016) typically find  $\theta_c < 15^\circ$  for their sample of long GRBs. Moreover, the fact that we do not observe a visible jet break in our observations up to  $\sim 8$  days after the burst may indeed be indicative of a large opening angle. While Wang et al. (2025a) propose a jet break near  $2 \times 10^5$  s and consequently find a smaller half-opening angle of  $\theta_j = 4.5_{-0.7}^{+1.0}^\circ$ , our observations are more complete at later times, in particular with the late EP observation to confirm the X-ray behavior, and do not support this angular model and evolution.

#### 4.4. Analytical discussion

A striking result from the analysis presented in Section 4.3 is the combination of a very high energy  $E_0 \sim 10^{56}$  erg and a very low  $\epsilon_B < 10^{-6}$ . Alternative parameter combinations with lower  $E_0$  and higher  $\epsilon_B$  would yield comparable luminosities and are more commonly observed in GRB afterglows. We found that this unusual combination is favored by the sampler because of (1) the absence of a clear break in the optical light curve, meaning  $\nu_m$  should be below the optical bands at early times, and (2) to accommodate for the passage of  $\nu_c$  in the X-rays around  $10^4$  s. In the slow cooling regime, these two elements place strong constraints on the possible parameter space. We note from our results that the viewing angle is close to or within the jet core. We can therefore, with good accuracy, look at analytical formulae in the standard top-hat, on-axis case. Following Panaitescu & Kumar (2000) and assuming that the emission is in the slow cooling regime, with  $\nu_c$  passing in the X-ray band at  $10^4$  s, we have the following four constraints:

- The model must reproduce the early time X-ray and optical temporal slope  $\alpha$ , which leads to a constraint on the injection slope  $p$ ,  $\alpha = \frac{3}{4}(p - 1)$ , for  $\nu_m < \nu < \nu_c$  in a constant-density ISM;
- The model must reproduce the normalization of the flux in the optical band, which gives a constraint on  $E_0$ ,  $n_{\text{ism}}$ ,  $\epsilon_e$  and  $\epsilon_B$  (Eq. B.7,  $F_\nu(t) \propto E_0^{(p+3)/4} n_{\text{ism}}^{1/2} \epsilon_e^{p-1} \epsilon_B^{-(p+1)/4} \nu^{-\beta} t^{-\alpha}$ ). By construction, this constraint combined with the value for  $p$  gives the correct normalization of the flux in X-rays before the break;
- The passage of  $\nu_c$  in the X-rays at  $10^4$  s gives a new constraint on  $E_0$ ,  $n_{\text{ism}}$  and  $\epsilon_B$  (Eq. 27,  $\nu_c \propto E_0^{-1/2} n_{\text{ism}}^{-1} \epsilon_B^{-3/2} t^{-1/2}$ );
- Because  $\nu_m$  only decreases with time, its value must be below the optical bands as early as the first data points considered, which gives another constraint on  $E_0$ ,  $\epsilon_e$  and  $\epsilon_B$  (Eq. 22,  $\nu_m \propto E_0^{1/2} \epsilon_e^2 \epsilon_B^{1/2} t^{-3/2}$ ).

Starting from the best-fit parameters, working on the three last conditions and the corresponding equations implies the following correlations to any change of  $E_0$ , so that the normalization, and the values of  $\nu_m$  and  $\nu_c$  are kept identical:

$$\begin{cases} \Delta \log(n_{\text{ism}}) = -5 \Delta \log(E_0) \\ \Delta \log(\epsilon_e) = -\Delta \log(E_0) \\ \Delta \log(\epsilon_B) = 3 \Delta \log(E_0) \end{cases} \quad (4)$$

Starting from  $\log_{10}(E_0) = 56.6$  (best-fit model), a lower value of  $\log_{10}(E_0) = 55$  maintaining these constraints would imply even

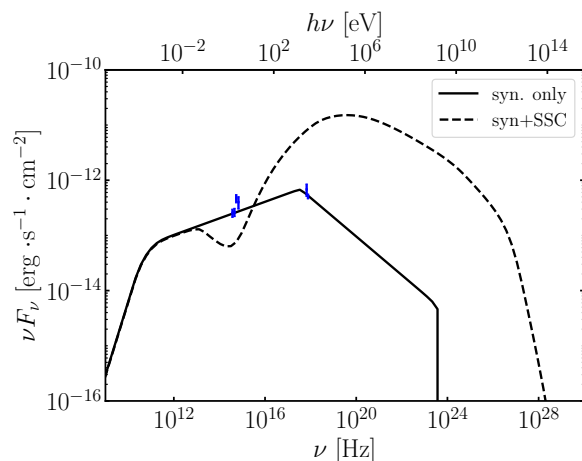


**Fig. 4.** Observed spectrum at  $t_{\text{obs}} = 8 \times 10^4$  s. The blue error bars show the fitted data points with  $7.5 \times 10^4$  s  $< t_{\text{obs}} < 8.5 \times 10^4$  s (optical and X-ray data). The solid curve represents the spectrum computed with the best-fit set of parameters found when SSC is not included in the model. The dashed curve represents the spectrum computed with the same parameters, this time including SSC.

more extreme values of  $\log_{10}(n_{\text{ism}}) = 10.6$ ,  $\log_{10}(\epsilon_e) = -1$  and  $\log_{10}(\epsilon_B) = -12$ . Such values are even more extreme and well outside our range of priors.

With a very low magnetization ( $\epsilon_B \lesssim 10^{-6}$ ), it is expected that SSC should strongly affect the emitted spectrum throughout the afterglow. We employ the model of PD24 to explore this effect.

To illustrate the potential importance of SSC scatterings on the model predictions, we performed a diagnostic test by taking the results from the fits presented in Section 4.3, and computing the afterglow emission, this time accounting for SSC scatterings. A new fit, this time including SSC emission, is presented in Section 4.5.

All models corresponding to the highest likelihood posterior are significantly affected by SSC. The corresponding light curves then fail to match the afterglow observations. An example with the set of parameters which provide the best fit without SSC is provided in Fig. 4. This spectrum is taken after the passage of  $\nu_c$  in the X-ray band, which can be seen as the second break in the spectrum (solid line).

We can understand this effect by looking at the model parameters. It is noteworthy that, in the fits without SSC,  $\epsilon_e/\epsilon_B > 10^4$  (see the light blue contours in Fig. D.1), which is an unusually high value and should lead to significant SSC emission. Indeed, if Klein-Nishina effects are ignored (SSC scatterings then occur only in the Thomson regime), then the ratio of SSC power to synchrotron power  $Y_{\text{noKN}} \sim \sqrt{\frac{\epsilon_e}{\epsilon_B}}$  in the fast cooling regime

and  $Y_{\text{noKN}} \sim \sqrt{\frac{\epsilon_e}{\epsilon_B}} \left( \frac{\gamma_m}{\gamma_c^{\text{syn}}} \right)^{\frac{p-2}{2}}$  in the slow cooling regime. In both cases,  $Y_{\text{noKN}} \gg 1$ . Even with the inclusion of Klein-Nishina corrections in PD24, the synchrotron emission is significantly altered, as shown in Fig. 4. In this example, SSC scatterings occur in the Thomson regime, and  $\nu_c$  is significantly lowered below the optical band, while all the emission in the X-rays and at higher energies is dominated by SSC.

We therefore deduce from this analytical study that the highest likelihood posterior values in the case without SSC radiation are highly constrained by three elements that are difficult to reconcile:

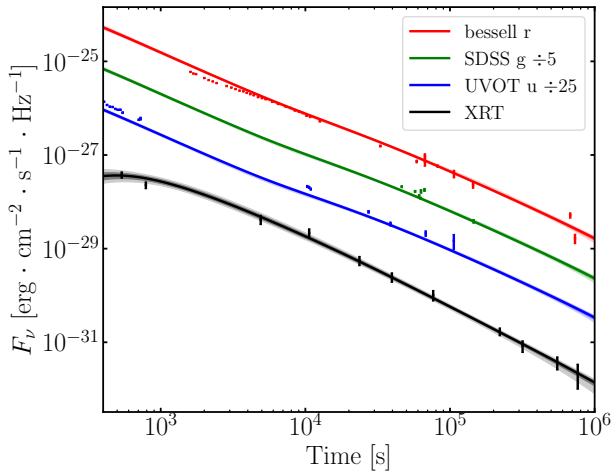


**Fig. 5.** Light curve fits from the inference with the afterglow model from Pellouin & Daigne (2024) for selected filters. Observed data and their errors are shown, and the solid line indicates the median value of the posterior sample at each time. The shaded contours correspond to the 68% and 95% quantiles of the posterior distribution.

(i) a high optical and X-ray luminosity, driving high  $E_0$  and  $n_{\text{ism}}$ , (ii)  $\nu_c$  passing in the X-ray band at  $\sim 10^4$  s while (iii)  $\nu_m$  is already below the optical bands at the earliest times (here 400 s), which strongly constrains the microphysics behind the shock. In addition, these sets of parameters (in particular, the high value of  $\epsilon_e/\epsilon_B$ ) imply strong SSC emission. This affects the predictions and limits the validity of any model that ignores SSC scatterings (see Fig. 4). We therefore use the model of PD24 in Section 4.5 to assess other potential types of solution to the afterglow of GRB 241030A.

#### 4.5. Results from PD24 – Synchrotron & SSC

In this section, we show the results of the fit to the afterglow data from 400 s post- $t_0$  with the PD24 model, including the effects of SSC and using the parameters and priors described in Section 4.2 and Table 1. The best fit light curves for this analysis are shown in Fig. 5. The posterior distribution for this fit are shown in Fig. D.1 (dark blue contours), and the 95% credible intervals for each parameters are given in the last column of Table 1.

With this analysis, we find a similar overall trend as found with NMMA/AFTERGLOWPY: the jet is very energetic,  $\log_{10}(E_0) = 56.2^{+0.7}_{-0.7}$ , and the jet opening angle is also large  $\theta_c = 9.7^{+0.3}_{-1.7}$ °, ramming against the upper limit of our prior. We again find very high external medium densities  $\log_{10}(n_{\text{ism}}) = 2.5^{+0.7}_{-0.7}$ . The analysis from PD24 suggests a lower value of  $\epsilon_e < 10^{-3}$ , and higher values of  $\log_{10}(\epsilon_B) = -4.17^{+0.76}_{-0.72}$ . These differences are likely driven by the inclusion of SSC in the model, which affects in particular the value of  $\nu_c$ .

The fitted data set includes two *Fermi*-LAT observations. We found that our afterglow model under-predicts the emission in this band. This is a consequence of the larger errors on these observations and of the low statistical weight of these two points on the whole data set, which the sampling algorithm does not seek to optimize as much as the optical and X-ray observations.

We observe from Fig. 5 that the multi-wavelength light curves are well reproduced by our analysis when SSC is included. However, as we show in Fig. 6, the X-ray LC is dominated by SSC emission, while the optical LC transitions through time from being synchrotron-dominated to SSC-dominated. This result is

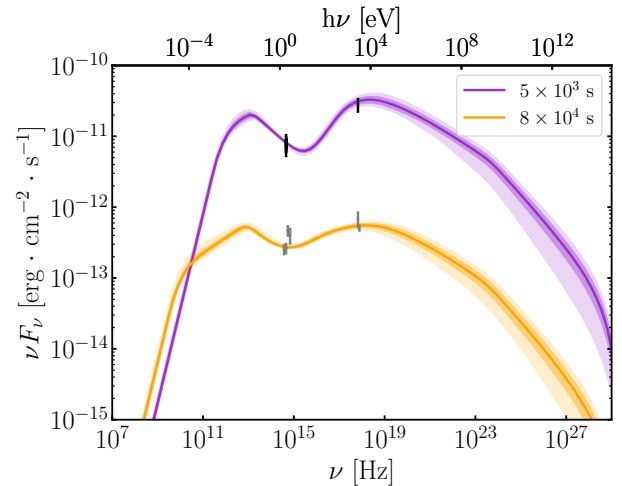


**Fig. 6.** Afterglow spectra at  $t_{\text{obs}} = 5 \times 10^3$  s (purple) and  $t_{\text{obs}} = 8 \times 10^4$  s (orange) computed with the model from Pellouin & Daigne (2024). The grey error bars show the fitted data points with  $4 \times 10^3$  s  $< t_{\text{obs}} < 6 \times 10^3$  s, while the black error bars show the fitted data points with  $7.5 \times 10^4$  s  $< t_{\text{obs}} < 8.5 \times 10^4$  s (optical and X-ray data). The shaded contours correspond to the 68% and 95% quantiles of the posterior distribution.

extremely unusual, and it is generally not expected that the X-ray emission be dominated by SSC. Overall, even the inclusion of SSC in the model does not resolve the tension detailed in Section 4.4 and the sampling algorithm still favors extreme parameter values which provide a good fit to the data, while corresponding to a scenario for the radiating mechanisms beyond usual assumptions for afterglow models.

## 5. Discussion

GRB 241030A is a long GRB with a high-luminosity afterglow. We presented a complete multi-wavelength data set of the afterglow observations from optical to X-rays, and covering epochs up to  $8 \times 10^5$  s ( $\sim 9.3$  days) post-trigger. In particular, we presented for the first time the observations from GRANDMA, KNC and COLIBRI. All optical/UV observations were processed in a consistent manner, and the consequences of line-of-sight extinction were coherently accounted for. Upon analysis of the optical images around the afterglow region, we did not find a host galaxy near the afterglow position, down to magnitudes  $i < 25.62$  and  $r < 25.82$ . This suggests a relatively faint host galaxy.

We conducted multi-wavelength Bayesian analyses of the afterglow of GRB 241030A with two physical models: AFTERGLOWPY (Ryan et al. 2020) within the NMMA Bayesian framework (Pang et al. 2023), and the model from Pellouin & Daigne (2024), which both assume radiation is emitted behind the forward shock of a structured jet, possibly viewed off-axis. Pellouin & Daigne (2024) also account for SSC scatterings. Our analyses conclusively show that this afterglow is powered by a highly energetic jet propagating in a high-density environment ( $n_{\text{ism}} \geq 10^2$  cm $^{-3}$ ). The absence of a clear multi-band jet break suggests that the emission is observed close to on-axis with a jet core angle ( $\theta_c \gtrsim 8^\circ$ ), and that the jet edges have not yet become visible within the observed time span.

Beyond these general results, our analyses faced some challenges. The overall afterglow luminosity is very high and resulted in fits with high isotropic kinetic energy equivalents  $E_0 \sim 10^{56}$  erg. The absence of a jet break in the afterglow data further points to a large jet opening angle, our analyses find

$\theta_c \approx 9^\circ$  which is close to the upper boundary of our Bayesian prior. These large estimates for the opening angles also lead to large values for the kinetic energy of the jet, of order  $10^{54}$  erg. Assuming that 1% of the ejecta energy is converted into the jet, this would imply that the rest-mass equivalent energy of several tens of Solar masses be dynamically ejected before jet launching.

If our assumption that the emission is powered by a population of electrons emitting synchrotron and SSC photons behind a forward shock is correct, then our results have strong consequences for the physical conditions of this afterglow. The very high jet kinetic energy is in contrast with the prompt emission energy, which is a relatively standard  $4 \times 10^{53}$  erg, implying unusually low values for the prompt emission efficiency  $\eta \lesssim 10^{-3}$ . Hence, GRB 241030A might be among a sample of a rare population of GRBs with very low prompt emission efficiency (Sarin et al. 2022; Ye et al. 2024; Li et al. 2025). Li et al. (2025) identified six afterglows discovered in optical-survey data between 2019 and 2023 with no detected prompt emission but with a measured redshift (between 1.06 and 2.9). Sarin et al. (2022) had modeled AT2020blt (ZTF20aajnksq) and AT2021any (ZTF21aaeyldq), giving an efficiency  $\lesssim 0.3$ – $4.5\%$  for AT2020blt. Ye et al. (2024) studied AT2021lfa (ZTF21aayokph) and gave an "exceptionally low radiation efficiency"  $\lesssim 0.02\%$ . Li et al. (2025) added AT2023lcr (ZTF23aaohpy) and gave an efficiency  $\lesssim 2.3\%$ . Note in addition that the initial jet Lorentz factor has values  $\Gamma_0 > 300$ , strongly rejecting the hypothesis of being in the 'dirty fireball' or 'failed gamma-ray burst' situation (Huang et al. 2002; Rhoads 2003). We also found unusually small values of  $\epsilon_e (< 10^{-2})$  and  $\epsilon_B (< 10^{-4})$ , and fits where  $\epsilon_e$  was fixed to a more canonical value of 0.1 were strongly disfavored. The combination of a very low magnetic energy fraction, a small electron energy fraction, and a large isotropic-equivalent kinetic energy suggests that the afterglow emission is largely adiabatic, with likely  $\lesssim 1\%$  of the total energy being radiated.

This first analysis, assuming no SSC scatterings, gave quantitatively good fits, but corresponds to an extreme case of an otherwise quite standard scenario to explain the afterglow light curve. The optical bands are at all times in the  $\nu_m < \nu < \nu_c$  regime, with a slow-cooling electron population. The X-rays are initially in the same regime and transition to  $\nu > \nu_c$  after  $t \sim 10^4$  s, leading to a mild steepening of the X-ray light curve. However, we found that the unusual physical parameters associated with the highest likelihood models lead in fact to a strong SSC contribution to the afterglow. When SSC is included, the resulting light curves and spectra with the same parameters fail to reproduce the observations.

We therefore relied on the model of Pellouin & Daigne (2024) to include SSC scatterings in the Thomson and Klein-Nishina regimes and conducted the same analysis. We found qualitatively similar results (a very energetic jet, seen within the jet core, with a large opening angle and unusually small values of  $\epsilon_e$  and  $\epsilon_B$ ). This time again, the multi-wavelength fit was satisfactory. However, in this scenario, we found a very strong SSC component, which is responsible for the emission in X-rays, and even down to the optical bands at late times. This scenario also challenges standard afterglow theory.

Analytical analysis in the synchrotron-only scenario suggested that these difficulties are due to the unusual combination of a very bright afterglow luminosity, the passage of  $\nu_c$  in the X-rays at  $10^4$  s, while simultaneously  $\nu_m$  remains below the optical bands even at the earliest times. These constraints impose unusually low values of  $\epsilon_B$ , which naturally imply a strong SSC component ( $Y_{\text{noKN}} \propto (\epsilon_e/\epsilon_B)^{1/2} (\gamma_m/\gamma_c^{\text{syn}})^{(p-2)/2}$ ). When SSC is included, solutions favor X-ray emission from the SSC compo-

nent, which releases the constraint on  $\nu_c$  but adds a new constraint to have very strong SSC emission. Therefore, the parameters differ slightly but the conclusions remain similar.

If the early-time optical afterglow emission is instead powered by another site (e.g. a reverse shock), then it is possible to release the constraint on  $\nu_m$  slightly. We performed another Bayesian fit with the model from Pellouin & Daigne (2024), this time assuming that the optical afterglow only starts after  $2 \times 10^4$  s. We still found results with the same qualitative properties already discussed here, which suggests that our findings are intrinsic to the afterglow of GRB 241030A. In addition, in such a scenario another difficulty would be to explain the smooth connection without temporal or spectral break between the early and late optical light curves, if there are indeed two different emitting regions or processes.

Our analysed data set contains observations from optical to X-rays, with high energy photons up to 2 GeV. To better constrain the physical scenario behind this unusual afterglow, radio observations would be particularly useful, as they would provide constraints in the lower-frequency part of the spectrum below  $\nu_m$ . This would therefore help constrain the value of  $\nu_m$  much better and thus clarify our conclusions. We also found that the *Fermi*-LAT observations did not contribute significantly to constrain the fit, but in such a scenario with strong SSC radiation, very high energy (VHE) observations around 1 TeV and by instruments such as the CTAO (Cherenkov Telescope Array Consortium et al. 2019) would provide very strong constraints on the SSC component and deepen our understanding of such afterglows.

## 6. Conclusions

In summary, GRB 241030A exhibited a very bright GRB afterglow compared to the vast majority of the population. This work presents deep observations of its emission from gamma rays to IR. This kind of (bright afterglow) GRB offers a chance to obtain well-sampled multi-wavelength afterglow light curves and thus an opportunity to conduct sophisticated analyses to constrain the GRB jet structure, environment, and afterglow emission model. We conducted both empirical and Bayesian analyses on the rich data of GRB 241030A which yielded extreme model parameters. They pointed to a powerful jet propagating in a dense medium, with isotropic-equivalent kinetic energies on the order of  $10^{56}$  erg and large jet angles, supported by the absence of a jet break within 8 days. If these parameters can be trusted, they impose strong conclusions about a very low prompt gamma-ray emission efficiency  $\eta \lesssim 10^{-3}$ , even when synchrotron self-Compton (SSC) effects are accounted for. In this scenario, the emission in X-rays is dominated by SSC, which is also non-standard and challenges our model assumptions. Our study shows that SSC scatterings play an important role in bright GRB afterglows and should be accounted for, but that even including this effect in our models may not be enough to reach a complete understanding of the radiative mechanisms in such events without complete spectral coverage of the afterglow observations from radio to very high energies. GRB 241030A might join the small but growing sample of long GRBs with low radiative efficiency.

## Paper writing team contributions

The global scientific research was equally led by J.-G. Ducoin and C. Pellouin. The Paper Writing Team (PWT) was coordinated by M. Pillas and N. Guessoum. Members of the PWT

were (in alphabetical order): D. Akl, S. Antier, J.-G. Ducoin, N. Guessoum, A. Holzmann Airasca, H. Koehn, N.L. Klinger, R. Z. Li, Y. Liang, F. Magnani, J. Mao, C. Pellouin, R. Pillera, N. Rakotondrainibe, Z. Wang. The internal review was conducted by F. Daigne, N. Guessoum, J. Mao, R. Gill.

## Acknowledgments

See details in the Appendix B.

## Data availability

Images and raw data are available upon request.

## References

- Abbott, B. P., others (LIGO Scientific Collaboration, & Collaboration), V. 2017, *ApJ*, 848, L13
- Aguilar-Ruiz, E., Gill, R., Beniamini, P., & Granot, J. 2025, arXiv e-prints, arXiv:2511.23349
- Aivazyan, V., Almualla, M., Antier, S., et al. 2022, *MNRAS*, 515, 6007
- Ajello, M., Arimoto, M., Axelsson, M., et al. 2019, *ApJ*, 878, 52
- Aksulu, M. D., Wijers, R. A. M. J., van Eerten, H. J., & van der Horst, A. J. 2022, *MNRAS*, 511, 2848
- Antier, S., Agayeva, S., Almualla, M., et al. 2020, *MNRAS*, 497, 5518
- Arnaud, K., Dorman, B., & Gordon, C. 1999, XSPEC: An X-ray spectral fitting package, Astrophysics Source Code Library, record ascl:9910.005
- Atwood, W., Albert, A., Baldini, L., et al. 2013, arXiv e-prints, arXiv:1303.3514
- Atwood, W. B., Abdo, A. A., Ackermann, M., et al. 2009, *ApJ*, 697, 1071
- Beniamini, P., Nava, L., & Piran, T. 2016, *MNRAS*, 461, 51
- Bertin, E. 2010, SWarp: Resampling and Co-adding FITS Images Together, Astrophysics Source Code Library, record ascl:1010.068
- Blanchard, P. K., Berger, E., & Fong, W.-f. 2016, *ApJ*, 817, 144
- Bloom, J. S., Frail, D. A., & Sari, R. 2001, *AJ*, 121, 2879
- Boquien, M., Burgarella, D., Roehly, Y., et al. 2019, *A&A*, 622, A103
- Bruel, P., Burnett, T. H., Digel, S. W., et al. 2018, Fermi-LAT improved Pass 8 event selection
- Cano, Z., Wang, S.-Q., Dai, Z.-G., & Wu, X.-F. 2017, *Advances in Astronomy*, 2017, 8929054
- Cen, R., Feng, L., & Ostriker, J. P. 2000, *ApJ*, 536, 195
- enko, S. B., Kelemen, J., Harrison, F. A., et al. 2008, *ApJ*, 677, 441
- Chambers, K. C., Magnier, E. A., Metcalfe, N., et al. 2016, arXiv e-prints, arXiv:1612.05560
- Chen, Y., Cui, W., Han, D., et al. 2021, in Society of Photo-Optical Instrumentation Engineers (SPIE) Conference Series, Vol. 11444, Society of Photo-Optical Instrumentation Engineers (SPIE) Conference Series, ed. J.-W. A. den Herder, S. Nikzad, & K. Nakazawa, 114445B
- Cheng, H., Zhang, C., Ling, Z., et al. 2025, *Experimental Astronomy*, 60, 15
- Cherenkov Telescope Array Consortium, Acharya, B. S., Agudo, I., et al. 2019, Science with the Cherenkov Telescope Array
- Cohen, E. & Piran, T. 1998, *ApJ*, 499, 301
- Collaboration, H., Bekhti, N. B., Flöer, L., et al. 2016, *Astronomy & Astrophysics*, 594, A116, arXiv:1610.06175 [astro-ph]
- Corre, D., Buat, V., Basa, S., et al. 2018, *A&A*, 617, A141
- de Barra, C., Meegan, C., & Fermi Gamma-ray Burst Monitor Team. 2024, GRB Coordinates Network, 38015, 1
- Del Vecchio, R., Dainotti, M. G., & Ostrowski, M. 2016, *ApJ*, 828, 36
- Evans, P. A., Beardmore, A. P., Page, K. L., et al. 2009, *MNRAS*, 397, 1177
- Evans, P. A., Beardmore, A. P., Page, K. L., et al. 2007, *A&A*, 469, 379
- Gaia Collaboration, Montegriffo, P., Bellazzini, M., et al. 2023, *AAP*, 674, A33
- Gehrels, N., Barthelmy, S. D., Burrows, D. N., et al. 2008, *ApJ*, 689, 1161
- Ghirlanda, G., Salafia, O. S., Paragi, Z., et al. 2018, *MNRAS*, 478, L18
- Gill, R. & Granot, J. 2023, *MNRAS*, 524, L78
- Goldstein, A., Connaughton, V., Briggs, M. S., & Burns, E. 2016, *ApJ*, 818, 18
- Goldstein, A. & others (Fermi GBM Collaboration 2017). 2017, *ApJ*, 848, L14
- Granot, J., Gompertz, B. P., Gill, R., & et al. 2018, *MNRAS*, 479, 1578
- Granot, J. & Sari, R. 2002, *ApJ*, 568, 820
- Greiner, J., Krühler, T., Klose, S., et al. 2015, *ApJ*, 809, 76
- Hallinan, G., Corsi, A., Mooley, K. P., & et al. 2017, *Science*, 358, 1579
- Hope, J. P., van Eerten, H. J., Kundu, S., & Schady, P. 2025, *MNRAS*, 538, 281
- Huang, Y. F., Dai, Z. G., & Lu, T. 2002, *MNRAS*, 332, 735
- Jayaraman, R., Fausnaugh, M. M., Vanderspek, R., & Ricker, G. R. 2024, GRB Coordinates Network, 38134, 1
- Jhavar, S., Wouters, T., Pang, P. T. H., et al. 2025, *Phys. Rev. D*, 111, 043046
- Kann, D. A., Agayeva, S., Aivazyan, V., et al. 2023, *ApJ*, 948, L12
- Kann, D. A., Klose, S., Zhang, B., et al. 2011, *ApJ*, 734, 96
- Kann, D. A., Klose, S., Zhang, B., et al. 2010, *ApJ*, 720, 1513
- Karpov, S. 2021, STDPipe: Simple Transient Detection Pipeline
- Karpov, S. 2025, *Acta Polytechnica*, 65, 50–64
- Klingler, N. J., Dichiara, S., Gupta, R., et al. 2024, GRB Coordinates Network, 37956, 1
- Kobayashi, S. 2000, *ApJ*, 545, 807
- Krimm, H. A., Barthelmy, S. D., Gupta, R., et al. 2024, GRB Coordinates Network, 38010, 1
- Lamb, G. P. & Kobayashi, S. 2017, *ApJ*, 850, 24
- Lang, D., Hogg, D. W., Mierle, K., Blanton, M., & Roweis, S. 2010, *AJ*, 139, 1782
- LHAASO Collaboration. 2023, *Science*, 380, 1390
- Li, M. L., Ho, A. Y. Q., Ryan, G., et al. 2025, *ApJ*, 985, 124
- Li, R.-Z., Lin, H., Li, S.-S., et al. 2024, GRB Coordinates Network, 38027, 1
- Liang, E.-W., Zhang, B., Zhang, B.-B., et al. 2018, *Nature Communications*, 9, 447
- Liang, Y. F., Jiang, S. Q., Hu, D. F., et al. 2024, GRB Coordinates Network, 38026, 1
- Lloyd-Ronning, N. M. & Zhang, B. 2004, *ApJ*, 613, 477
- MAGIC Collaboration, Acciari, V. A., Ansoldi, S., et al. 2019a, *Nature*, 575, 455
- MAGIC Collaboration, Acciari, V. A., Ansoldi, S., et al. 2019b, *Nature*, 575, 459
- McCarthy, I. G. & Laskar, T. 2024, *ApJ*, 970, 135
- Mészáros, P. & Rees, M. J. 1997, *ApJ*, 476, 232
- Mészáros, P., Rees, M. J., & Wijers, R. A. M. J. 1998, *ApJ*, 499, 301
- Moskvitin, A. S., Goranskij, V. P., & GRB follow-up Team. 2024, GRB Coordinates Network, 38016, 1
- Nakar, E., Ando, S., & Sari, R. 2009, *ApJ*, 703, 675
- Nysewander, M., Fruchter, A. S., & Pe'er, A. 2009, *ApJ*, 701, 824
- O'Connor, B., Troja, E., Ryan, G., et al. 2023, *Science Advances*, 9, eadi1405
- Pal, A., Dafcikova, M., Ripa, J., et al. 2024, GRB Coordinates Network, 38074, 1
- Panaitecu, A. & Kumar, P. 2000, *ApJ*, 543, 66
- Panaitecu, A. & Kumar, P. 2003, *ApJ*, 592, 390
- Pang, P. T. H. et al. 2023, *Nature Commun.*, 14, 8352
- Pei, Y. C. 1992, *ApJ*, 395, 130
- Pellouin, C. & Daigne, F. 2024, *Astron. Astrophys.*, 690, A281
- Perley, D. A., Krühler, T., Schulze, S., et al. 2016a, *ApJ*, 817, 7
- Perley, D. A., Niino, Y., Tanvir, N. R., Vergani, S. D., & Fynbo, J. P. U. 2016b, *Space Sci. Rev.*, 202, 111
- Pillera, R., Gupta, R., Kocevski, D., Loizzo, P., & Fermi-LAT Collaboration. 2024, GRB Coordinates Network, 37979, 1
- Piran, T. 1999, *Phys. Rep.*, 314, 575
- Piran, T. 2004, *Reviews of Modern Physics*, 76, 1143
- Planck Collaboration, Aghanim, N., Akrami, Y., et al. 2020, *A&A*, 641, A6
- Racusin, J. L. et al. 2011, *ApJ*, 738, 138
- Rakotondrainibe, N. A., Buat, V., Turpin, D., et al. 2024, *A&A*, 690, A373
- Rhoads, J. E. 2003, *ApJ*, 591, 1097
- Ridnaia, A., Frederiks, D., Lysenko, A., et al. 2024, GRB Coordinates Network, 37982, 1
- Roming, P. W. A., Kennedy, T. E., Mason, K. O., et al. 2005, *Space Sci. Rev.*, 120, 95
- Ryan, G., van Eerten, H., Piro, L., & Troja, E. 2020, *ApJ*, 896, 166
- Sari, R. & Esin, A. A. 2001, *ApJ*, 548, 787
- Sari, R. & Piran, T. 1999, *ApJ*, 520, 641
- Sari, R., Piran, T., & Halpern, J. P. 1999, *ApJ*, 519, L17
- Sari, R., Piran, T., & Narayan, R. 1998, *ApJ*, 497, L17
- Sarin, N., Hamburg, R., Burns, E., et al. 2022, *MNRAS*, 512, 1391
- Schady, P., Dwelly, T., Page, M. J., et al. 2012, *A&A*, 537, A15
- Schlafly, E. F. & Finkbeiner, D. P. 2011, *ApJ*, 737, 103
- Schneider, B., Mo, G., Juneau, J., et al. 2024, GRB Coordinates Network, 38021, 1
- SVOM/C-GFT Team, WU, C., Kang, Z., et al. 2024, GRB Coordinates Network, 37970, 1
- SVOM/GRM Team, Wang, Y., Wang, C.-W., et al. 2024, GRB Coordinates Network, 37972, 1
- Tosta e Melo, I., Ducoin, J. G., Vidadi, Z., et al. 2024, *A&A*, 682, A141
- Troja, E., Piro, L., van Eerten, H., & et al. 2017, *Nature*, 551, 71
- Varun, Zhang, B.-B., Zhao, X.-H., et al. 2025, arXiv e-prints, arXiv:2510.24864
- Vianello, G., Lauer, R. J., Younk, P., et al. 2015, The 34th International Cosmic Ray Conference (ICRC), 30 July-6 August, 2015, The Hague, The Netherlands, arXiv:1507.08343
- Wang, C.-J., Bai, J.-M., Fan, Y.-F., et al. 2019, *Research in Astronomy and Astrophysics*, 19, 149
- Wang, Q. L., Wang, Y., Wang, H., et al. 2024, GRB Coordinates Network, 38055, 1
- Wang, Q.-L., Zhou, H., Wang, Y., et al. 2025a, *ApJ*, 987, 129
- Wang, Z., Wang, C., Gao, H., et al. 2025b, arXiv e-prints, arXiv:2510.17323
- Willingale, R., Starling, R. L. C., Beardmore, A. P., Tanvir, N. R., & O'Brien, P. T. 2013, *MNRAS*, 431, 394, arXiv:1303.0843 [astro-ph]

- Wood, M., Caputo, R., Charles, E., et al. 2017, PoS, ICRC2017, 824
- Wu, H. Z., Wang, B. T., Hu, D. F., et al. 2024, GRB Coordinates Network, 37997, 1
- Xin, Y.-X., Bai, J.-M., Lun, B.-L., et al. 2020, *Research in Astronomy and Astrophysics*, 20, 149
- Ye, X.-M., Wei, D.-M., Zhu, Y.-M., & Jin, Z.-P. 2024, *Research in Astronomy and Astrophysics*, 24, 045011
- Yuan, W., Zhang, C., Chen, Y., & Ling, Z. 2022, *The Einstein Probe Mission* (Springer Nature Singapore), 1–30
- Zheng, W., Brink, T. G., Filippenko, A. V., Yang, Y., & KAIT GRB Team. 2024, GRB Coordinates Network, 37959, 1
- 
- 1 Aix-Marseille Univ., CNRS/IN2P3, Ctr. de Physique des Particules de Marseille, IPhU (France)
- 2 The Raymond and Beverly Sackler School of Physics and Astronomy, Tel Aviv University, Tel Aviv 69978, Israel
- 3 E.Kharadze Georgian National Astrophysical Observatory, Mt. Kanobili, Abastumani, 0301 Adigeni, Georgia
- 4 Samtskhe-Javakheti State University, Akhaltsikhe, Georgia
- 5 Université de la Côte d’Azur, Nice, France
- 6 Center for Astrophysics and Space Science (CASS), New York University Abu Dhabi, Saadiyat Island, PO Box 129188, Abu Dhabi, UAE
- 7 New York University Abu Dhabi, PO Box 129188, Saadiyat Island, Abu Dhabi, UAE
- 8 Instituto de Astronomía, Universidad Nacional Autónoma de México, Apartado Postal 70-264, 04510 México, CDMX, México
- 9 School of Physics and Astronomy, University of Minnesota, Minneapolis, MN 55455, USA
- 10 IJCLab, Univ Paris-Saclay, CNRS/IN2P3, Orsay, France
- 11 IRAP, Université de Toulouse, CNRS, CNES, UPS, France
- 12 Aix Marseille Univ., CNRS, CNES, LAM, Marseille, France
- 13 Department of Applied Physics and Astronomy, and Academy for Astronomy, Space Sciences and Technology, University of Sharjah, Sharjah, United Arab Emirates
- 14 Oukaimeden Observatory and High Energy Physics, Astrophysics and Geoscience Laboratory, FSSM, Cadi Ayyad University, Marrakesh, Morocco
- 15 Dipartimento Interateneo di Fisica, Politecnico di Bari, Via E. Orabona 4, 70125, Bari, Italy
- 16 Istituto Nazionale de Fisica Nucleare (INFN) — Sezione di Bari, 70126 Bari, Italy
- 17 Mullard Space Science Laboratory - University College London
- 18 Department of Physics & Astronomy, Louisiana State University, Baton Rouge, LA 70803, USA
- 19 School of Earth and Space Exploration, Arizona State University, PO Box 871404, Tempe AZ 85287, USA
- 20 Sorbonne Université, CNRS, UMR 7095, Institut d’Astrophysique de Paris, 98 bis boulevard Arago, 75014 Paris, France
- 21 Institute of Physics and Astronomy, Theoretical Astrophysics, University Potsdam, Haus 28, Karl-Liebknecht-Str. 24/25, 14476
- 22 Max Planck Institute for Gravitational Physics (Albert Einstein Institute), Am Mühlenberg 1, Potsdam 14476, Germany
- 23 Cahill Center for Astrophysics, California Institute of Technology, MC 249-17, 1216 E California Boulevard, Pasadena, CA, 91125, USA
- 24 Université Paris Cité, CNRS, Astroparticule et Cosmologie, F-75013 Paris, France
- 25 KNC, Volkssternwarte Paderborn, Im Schlosspark 13, 33104
- 26 National Research Institute of Astronomy and Geophysics (NRIAG), 1 El-marsad St., 11421 Helwan, Cairo, Egypt
- 27 Xinjiang Astronomical Observatory, Chinese Academy of Sciences, Urumqi, Xinjiang, 830011, China
- 28 School of Astronomy and Space Science, University of Chinese Academy of Sciences, Beijing 100049, China
- 29 School of Physics and Astronomy, University of Leicester, Leicester, UK
- 30 Observatorio de Calar Alto, Sierra de los Filabres, Gérgal, Almería 04550, Spain
- 31 Osservatorio Astronomico di Brera, via E. Bianchi 46, I-23807 Merate (LC), Italy
- 32 KNC, AAVSO, Hidden Valley Observatory(HVO), Colfax, WI, USA
- 33 Instituto de Radioastronomía y Astrofísica, Universidad Nacional Autónoma de México, Antigua Carretera a Pátzcuaro # 8701, Ex-Hda. San José de la Huerta, Morelia, Michoacán, México C.P. 58089, Mexico
- 34 Instituto de Astronomía, Universidad Nacional Autónoma de México, km 107 Carretera Tijuana-Ensenada, 22860 Ensenada, Baja California, México
- 35 American University of Sharjah, Physics Department, PO Box 26666
- 36 University of Trento, Via Calepina, 14, 38122 Trento TN, Italy
- 37 Purple Mountain Observatory, Chinese Academy of Sciences, Nanjing 210023, China
- 38 School of Astronomy and Space Sciences, University of Science and Technology of China, Hefei 230026, China
- 39 National Astronomical Observatories, Chinese Academy of Sciences, Beijing 100101, China
- 40 School of Astronomy and Space Science, University of Chinese Academy of Sciences, Beijing 100049, China
- 41 Institute for Frontier in Astronomy and Astrophysics, Beijing Normal University, Beijing 102206, China
- 42 FZU - Institute of Physics of the Czech Academy of Sciences, Na Slovance 1999/2, CZ-182 21, Praha, Czech Republic
- 43 Astrophysics Science Division, NASA Goddard Space Flight Center, Mail Code 661, Greenbelt, MD 20771, USA
- 44 Center for Space Sciences and Technology, University of Maryland, Baltimore County, Baltimore, MD 21250, USA
- 45 Center for Research and Exploration in Space Science and Technology, NASA/GSFC, Greenbelt, Maryland 20771, USA
- 46 KNC, K26 / Contern Observatory (private obs.), 1, beim Schmilberbour, 5316 Contern, Luxembourg
- 47 KNC, Institut Polytechnique des Sciences Avancées: Ivry-sur-Seine, Île-de-France, FR
- 48 Physics Department, Tsinghua University, Beijing, 100084, China
- 49 Instituto de Ciencias Nucleares, Universidad Nacional Autónoma de México, Apartado Postal 70-264, 04510 México, CDMX, Mexico
- 50 Yunnan Observatories, Chinese Academy of Sciences, Kunming 650216, People’s Republic of China
- 51 Center for Astronomical Mega-Science, Chinese Academy of Sciences, Beijing 100012, People’s Republic of China
- 52 Key Laboratory for the Structure and Evolution of Celestial Objects, Chinese Academy of Sciences, Kunming 650216, People’s Republic
- 53 Facultad de Ciencias, Universidad Nacional Autónoma de México, Apartado Postal 70-264, 04510 México, CDMX, México
- 54 Institute of Astronomy and NAO, Bulgarian Academy of Sciences, 72 Tsarigradsko Chaussee Blvd., 1784 Sofia, Bulgaria
- 55 National Astronomical Research Institute of Thailand (NARIT)
- 56 KNC, International Astronomical Center, Abu Dhabi, UAE
- 57 W.W. Hansen Experimental Physics Laboratory, Kavli Institute for Particle Astrophysics and Cosmology, Department of Physics and SLAC National Accelerator Laboratory, Stanford University, Stanford, CA 94305, USA
- 58 Université de Strasbourg, CNRS, IPHC UMR 7178, F-67000 Strasbourg, France
- 59 Ulugh Beg Astronomical Institute, Uzbekistan Academy of Sciences, Astronomy str. 33, Tashkent 100052, Uzbekistan
- 60 KNC, AAVSO Observer; Pobedy Street, House 7, Flat 60, Yuzhno-Morskoy, Nakhodka, Primorsky Krai 692954, Russia
- 61 Main Astronomical Observatory of the National Academy of Sciences of Ukraine, 27 Akademik Zabolotny St., Kyiv, 03143, Ukraine
- 62 KNC, Société Astronomique de France, Observatoire de Dauban, FR 04150 Banon, France
- 63 Astronomical Observatory, Taras Shevchenko National University of Kyiv, 3 Observatorna St., 04053 Kyiv, Ukraine
- 64 Department of Physics, University of Aberdeen, Aberdeen AB24 3UE, UK
- 65 Université Paris-Saclay, Université Paris Cité, CEA, CNRS, AIM, 91191, Gif-sur-Yvette, France
- 66 Yunnan Observatories, Chinese Academy of Sciences, 650216 Kunming, Yunnan Province, People’s Republic of China
- 67 University of Chinese Academy of Sciences, Beijing 100049, China

<sup>68</sup> Department of Astronomy, Tsinghua University, Beijing 100084, China

<sup>69</sup> Department of Astronomy, School of Physics, Huazhong University of Science and Technology, Luoyu Road 1037, Wuhan 430074, China

<sup>70</sup> Key Laboratory of Particle Astrophysics, Institute of High Energy Physics, Chinese Academy of Sciences, Beijing 100049, China

## Appendix A: Additional Contributions

**Paper writing team** The global scientific research was equally led by J.-G. Ducoin and C. Pellouin. The Paper Writing Team was coordinated by M. Pillas and N. Guessoum. Members of the Paper Writing Team were in alphabetical order: D. Akl, S. Antier, J.-G. Ducoin, N. Guessoum, A. Holzmann Airasca, H. Koehn, N.L. Klinger, R. Z. Li, Y. Liang, F. Magnani, J. Mao, C. Pellouin, R. Pillera, N. Rakotondrainibe, Z. Wang. The internal review was conducted by F. Daigne, N. Guessoum, J. Mao. Runs on the interpretation were performed by C. Pellouin and H. Koehn in particular.

**Image processing** Data analysis of the images were performed by D. Akl, S. Antier, E. de Bruin, J.-G. Ducoin, P.-A. Duverne, S. Karpov, N. Kochiashvili, M. Mašek, M. Pillas, D. Turpin. GRANDMA operations were carried out by C. Douzet, P.-A. Duverne, T. Du Łaż, T. Hussenot, A. Le Calloch, M. Mašek, N. Kochiashvili, Y. Rajabov, M. Tanasan, with assistance of the core-team: C. Andrade, S. Antier, M. Coughlin, P.-A. Duverne, P. Hello, N. Guessoum, S. Karpov, T. Pradier, D. Turpin.

**Observations** Members of the AbAO team that contributed to observations are V. Aivazyan, R. Inasaridze, N. Kochiashvili. Observations with AbAO-T150 were made by T. Kvernadze. Members of the CFHT team that contributed to observations are S. Antier and M. Pillas. Members of the COLIBRÍ (outside of GRANDMA members) that contributed to observations are C. Angulo, J.-L. Atteia, S. Basa, R.-L. Becerra, D. Dornic, F. Fortin, L. Garcia, R. Gill, N. Globus, W. Lee, D. Lopez-C. Camara, E. Moreno Méndez, M. Pereyra, D. Ramírez, A.M. Watson. Members of the FRAM team that contributed to observations are S. Karpov, M. Mašek. Members of the GTC team that contributed to observations are F. Agui Fernandez, A. de Ugarte Postigo. Members of the KAO team that contributed to observations are G. Hamed, E. Elhosseiny, R. Mabrouk, M. Mohlam, A. Takey. Members of the HAO team that contributed to observations are Z. Benkhaldoun, A. Kaeouach. Members of the NAO team that contributed to observations are B.M. Mihov, L. Slavcheva-Mihova. Members of the TAROT team that contributed to observations are S. Antier, A. Klotz, C. Limonta. Members of the TRT team that contributed to observations are K. Noysena, M. Tanasan, K.S. Tinyanont. Members of the TNOT that contributed to observations are A. Esadmdin, A. Iskandar, J. Liu, H. Peng, L.T. Wang, X.F. Wang, Y.S. Yan. Members of the GMG that contributed to observations are J. Mao and R. Z. Li.

Members of the kilonova-catcher program of GRANDMA that contributed to observations are C. Andrede, M. Freeberg, H.B. Eggenstein; R. Kneip; A. Lekic; M. Odeh; M. Serrau; D. Turpin.

Members that contributed to the Einstein Probe team are Y. Liang (Einstein Probe representative for this work), C.C. Jin, H. Sun, D.F. Hu, S.Q. Jiang, B.T. Wang, H.Z. Wu, Q.Y. Wu, H.N. Yang, X.F. Wang, W. Yuan, H.S. Zhao, J.J. Xu.

Members that contributed to the Fermi/LAT team are E. Bissaldi; A. Holzmann Airasca; N. Omodei; R. Pillera.

Members that contributed to the Swift/BAT team are A. Breeveld; P.A. Evans; M. Ferro coordinated by N. Klingler.

**Bayesian analysis** Runs on the interpretation were performed by C. Pellouin and H. Koehn in particular.

## Appendix B: Acknowledgments (details)

M.W. C. acknowledges support from the National Science Foundation with grant numbers PHY-2117997, PHY-2308862 and PHY-2409481. N. G. acknowledges the support of the Simons Foundation (MP-SCMPS-00001470, N. G.). H. K. acknowledges funding from the European Union (ERC, SMArt, 101076369). N. J. K. acknowledges support by NASA under award number 80GSFC24M0006. J. M. acknowledges support by the National Key R&D Program of China (2023YFE0101200), Natural Science Foundation of China 12393813, and the Yunnan Revitalization Talent Support Program (YunLing Scholar Project). C. P. acknowledges support by consolidator ERC grant 818899 (JetNS). A.M. W. acknowledges support by UNAM/DGAPA project IN109224. The NRIAG team acknowledges financial support from the Egyptian Science, Technology & Innovation Funding Authority (STDF) under grant number 45779. B.M. M. and L. S.-M. acknowledge support from the infrastructure purchased/renovated under the National Roadmap for Research Infrastructure (2020-2027), financially coordinated by the Ministry of Education and Science of Republic of Bulgaria (agreement D01-326/04.12.2023). M. M. and S. K. acknowledge support by MEYS (Czech Republic) under the projects Czech Republic MEYS LM2023032, LM2023047, and CZ.02.01.01/00/22\_008/0004632. The COLIBRÍ team acknowledges support of the staff of the Observatorio Astronómico Nacional on the Sierra de San Pedro Mártir and the COLIBRÍ and DDRAGO engineering teams.

AbAO team acknowledges Shota Rustaveli National Science Foundation of Georgia (SRNSFG, grant FR-24-7713). E. B., A. H. A., N. O. and R. P. acknowledge support for LAT development, operation and data analysis from NASA and DOE (United States), CEA/Irfu and IN2P3/CNRS (France), ASI and INFN (Italy), MEXT, KEK, and JAXA (Japan), and the K.A. Wallenberg Foundation, the Swedish Research Council and the National Space Board (Sweden). This work is also supported in the operations phase from INAF (Italy), and CNES (France) is also gratefully acknowledged. This work was performed in part under the DOE Contract DEAC02-76SF00515. This work is partly based on data obtained with the CFH/Megacam instrument, and the ACME is thanked for providing necessary time for this work. COLIBRÍ received support from the French government under the France 2030 investment plan, as part of the Initiative d'Excellence d'Aix-Marseille Université-A\*MIDEX through (ANR-11-LABX-0060 - OCEVU) and (AMX-19-IET-008 - IPhU), from LabEx FOCUS (ANR-11-LABX-0013), From Centre National d'Etudes Spatiales (CNES) and from CSAA-INSU-CNRS support program, and in Mexico from UNAM (Secretaria Administrativa, Coordinacion de la Investigacion Cientifica, Instituto de Astronomia and PAPIIT grant IN105921), and SECIHTI/CONACyT (277901, Ciencias de Frontera 1046632 and Laboratorios Nacionales). This work is also partly based on data obtained with the instrument OSIRIS, built by a Consortium led by the Instituto de Astrofísica de Canarias in collaboration with the Instituto de Astronomía of the Universidad Autónoma de México. OSIRIS was funded by GRANTECAN and the National Plan of Astronomy and Astrophysics of the Spanish Government. This work is finally based on observations made with the Thai Robotic Telescope under program ID TRTC12A\_001, which is operated by the National Astronomical Research Institute of Thailand (Public Organization). CFH and Skyportal are part of a project that has received funding from the European Union's Horizon Europe Research and innovation programme under Grant Agreement No 101131928. This project

is based on observations obtained with MegaPrime/MegaCam, a joint project of CFHT and CEA/DAPNIA, at the Canada-France-Hawai'i Telescope (CFHT) which is operated by the National Research Council (NRC) of Canada, the Institut National des Sciences de l'Univers of the Centre National de la Recherche Scientifique (CNRS) of France, and the University of Hawai'i. C. D. acknowledges funding from the European Union's Horizon Europe Research and Innovation Programme under Grant Agreement No 101131928 (ACME project).

The *Fermi* LAT Collaboration acknowledges generous ongoing support from a number of agencies and institutes that have supported both the development and the operation of the LAT as well as scientific data analysis. These include the National Aeronautics and Space Administration and the Department of Energy in the United States, the Commissariat à l'Énergie Atomique and the Centre National de la Recherche Scientifique / Institut National de Physique Nucléaire et de Physique des Particules in France, the Agenzia Spaziale Italiana and the Istituto Nazionale di Fisica Nucleare in Italy, the Ministry of Education, Culture, Sports, Science and Technology (MEXT), High Energy Accelerator Research Organization (KEK) and Japan Aerospace Exploration Agency (JAXA) in Japan, and the K. A. Wallenberg Foundation, the Swedish Research Council and the Swedish National Space Board in Sweden.

Additional support for science analysis during the operations phase is gratefully acknowledged from the Istituto Nazionale di Astrofisica in Italy and the Centre National d'Études Spatiales in France. This work performed in part under DOE Contract DE-AC02-76SF00515.

### Appendix C: Details about Fermi-LAT data reduction

For the LAT analysis we followed the standard approach (as described in Ajello et al. 2019) using the “P8R3” (Atwood et al. 2013; Bruel et al. 2018) processed events. Specifically, we employed the P8R3\_TRANSIENT\_010E event class, during the time interval where we have significant detections, which is optimized for transient source analysis, along with the corresponding instrument response functions<sup>5</sup>. For the extended emission search, we used the cleaner class P8R3\_SOURCE.

Events were chosen within the time interval from  $t_0$  to  $t_0 + 13$ ks covering the energy range from 100 MeV to 100 GeV in a region of  $10^\circ$  centered on the UVOT position. For the spectral analysis we used “Multi-Mission Maximum Likelihood” (ThreeML) (Vianello et al. 2015), a python-based software package for parameter inference with maximum likelihood, that provides an interface to the instrument response files and data in plugins. For the LAT data, two different plugins are available: FermiLATLike for unbinned analysis (which interfaces with *gtburst*<sup>6</sup>, part of the *fermitools*<sup>7</sup>), and FermipyLike for binned likelihood analysis with an interface to *fermipy* (Wood et al. 2017). The results of the time resolved spectral analysis are shown in Table C.1.

We performed an unbinned likelihood analysis of the burst spanning from  $t_0$  to  $t_0 + 800$ s, using the FermiLATLike plugin, using the P8R3\_TRANSIENT\_010E event class. This analysis returned a test-statistic value of  $TS \sim 49$ , corresponding to a

<sup>5</sup> <http://www.slac.stanford.edu/exp/glast/groups/canda/latPerformance.htm>

<sup>6</sup> <https://fermi.gsfc.nasa.gov/ssc/data/analysis/scitools/gtburst.html>

<sup>7</sup> <https://github.com/fermi-lat/Fermitools-conda/>

significance  $\sigma \sim 7$ , using  $\sigma \sim \sqrt{TS}$ . The result of the spectral analysis is displayed in Fig. C.1.

Interval	Flux (MeV s <sup>-1</sup> cm <sup>-2</sup> )	Spec. index	TS	Class
$T - T_0$ [s]	0.1 - 10 GeV	$\Gamma$		
1.2 - 292	$(1.0^{+1.2}_{-0.5}) \times 10^{-3}$	$-2.60^{+0.78}_{-0.82}$	11.3	T
292 - 403	$(4.2^{+4.9}_{-2.0}) \times 10^{-3}$	$-1.91^{+0.49}_{-0.48}$	10.4	T
403 - 556	$(2.8^{+3.2}_{-1.3}) \times 10^{-3}$	$2.0^{+0.46}_{-0.46}$	22.8	T
556 - 767	$(3.3^{+2.4}_{-1.2}) \times 10^{-3}$	$-2.03^{+0.38}_{-0.37}$	21.8	T
5.3k - 7.1k	$< 1.7 \times 10^{-3}$	-2.50	1.18	S
9.7k - 13k	$< 5.2 \times 10^{-4}$	-2.50	0.39	S
15.5k - 22.7k*	$< 1.1 \times 10^{-5}$	-2.50	-0.34	S
22.7k - 33.1k*	$< 1.2 \times 10^{-5}$	-2.50	-0.25	S
33.1k - 48.4k*	$< 1.1 \times 10^{-5}$	-2.50	-0.57	S
48.4k - 70.6k*	$< 1.0 \times 10^{-5}$	-2.50	-0.50	S
70.6k - 103.1k*	$< 4.0 \times 10^{-4}$	-2.50	0.82	S
103.1k - 150.6k*	$< 6.0 \times 10^{-4}$	-2.50	0.34	S
150.6k - 219.9k*	$< 1.0 \times 10^{-5}$	-2.50	-0.73	S
219.9k - 321.2k*	$< 1.0 \times 10^{-5}$	-2.50	-1.07	S
321.2k - 469.0k*	$< 9.9 \times 10^{-5}$	-2.50	1.98	S
469.0k - 684.8k*	$< 1.1 \times 10^{-5}$	-2.50	-2.21	S

**Table C.1.** Time-resolved spectral analysis of GRB 241030A with LAT. The symbol \* indicates a binned analysis (unbinned otherwise). A detection is considered significant in case of  $TS > 9$ . For upper limits, the spectral index has been fixed to -2.50. The event class "T" refers to P8R3\_TRANSIENT\_010E, and "S" refers to P8R3\_SOURCE.

### Appendix D: Posterior corner plot for the Bayesian analyses

We show the posterior corner plots from the inferences in Section 4 in Fig. D.1.

### Appendix E: Observational campaign

GRB 241030A was detected at  $t_0 = 05:48:03$  UT on 2024 October 30 ( $T_{90} = 166$  s in 50–300 keV) by the *Fermi* Gamma-ray Burst Monitor (GBM, de Barra et al. 2024). It was also independently detected by *Konus-Wind* (KW, Ridnaia et al. 2024) at 2024-10-30 05:49:56 in the 18 keV–1 MeV band ( $T_{90} = 211$  s), by *Gamma-Ray Burst Alpha* (GRBAlpha, Pal et al. 2024) at 2024-10-30 05:50 in the 80–950 keV band ( $T_{90} = 208$  s), by the *SVOM* Gamma-Ray Monitor (GRM) at 2024-10-30 05:48:14 in the 15 keV–5 MeV range (SVOM/GRM Team et al. 2024), and by the *Neil Gehrels Swift Observatory* (Swift) Burst Alert Telescope (BAT, Klingler et al. 2024) in the 15–150 keV band ( $T_{90} = 173$  s, Krimm et al. 2024). Further characteristics of its prompt emission are described in Wang et al. (2025a); Varun et al. (2025).

The optical counterpart was rapidly detected by the *Swift* Ultraviolet/Optical Telescope (UVOT), providing an accurate posi-

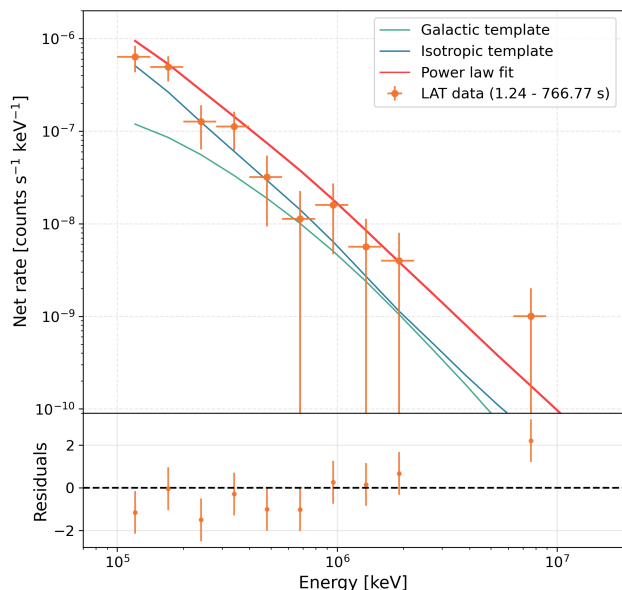


**Fig. C.1.** Fermi-LAT count spectrum (in counts  $s^{-1} \text{keV}^{-1}$ ) and residuals (in sigma units) for the PL model for the time integrated analysis.

tion of the event (RA = 343.13987, DEC = 80.44996, 0.61 arcsec uncertainty, Klingler et al. 2024) thanks to *Swift*'s rapid slewing capabilities (Romig et al. 2005). As mentioned in Wang et al. (2024), the UVOT instrument covered part of the UV and optical prompt emission as observations started 80s post- $t_0$ . This prompt sequence was followed by a multi-wavelength campaign in the hard X-ray, soft X-ray, optical, and infrared bands, including: the *Transiting Exoplanet Survey Satellite* (TESS, Jayaraman et al. 2024), the *COSMOS-8k* camera onboard the 1-m telescope at Palomar (Schneider et al. 2024), the Special Astrophysical Observatory of the Russian Academy of Sciences (SAO RAS, Moskvitin et al. 2024), and the *SVOM* Chinese Ground Follow-up Telescope (C-GFT, SVOM/C-GFT Team et al. 2024).

In this work, we collected data from many facilities. First, the GRB afterglow was detected at high energies by the *Fermi* Large Area Telescope (LAT, Pillera et al. 2024). In X-rays, the Wide-field X-ray Telescope (WXT, Wu et al. 2024) and the Follow-up X-ray Telescope (FXT, Liang et al. 2024) onboard the *Einstein Probe* (EP, Yuan et al. 2022), together with the *Swift*-XRT, also detected the X-ray afterglow (Klingler et al. 2024). On the ground, we can cite in particular the Global Rapid Advanced Network for Multi-messenger Addicts (GRANDMA; Antier et al. 2020; Aivazyan et al. 2022; Kann et al. 2023; Tosta e Melo et al. 2024) network, which includes contributions from the Abastumani Observatory 70-cm telescope and 1.5m telescope (AbAO-T70, AbAO-T150), the MegaCam instrument onboard the Canada–France–Hawaii Telescope (CFHT), the F/(Ph)otometric Robotic Atmospheric Monitor (FRAM), the Gran Telescopio Canarias with the Optical System for Imaging and low-Intermediate-Resolution Integrated Spectroscopy (GTC/OSIRIS), the 50-cm telescope of the High Atlas Observatory (HAO), the 2-m telescope of the Kottamia Astronomical Observatory (KAO), the 1.5-m AZ1500 and 2-m telescopes of the Rozhen National Astronomical Observatory of Bulgaria (NAO-1.5m, NAO-2m), the Thai Robotic Telescope at Sierra Remote Observatories (TRT/SRO),

the Telescope à Actions Rapides of Calern (TAROT/TCA), and the 80-cm Tsinghua-Nanshan Optical Telescope (TNOT). This network during the follow-up was also associated with the COLIBRÍ telescope, equipped with the commissioning camera named OGSE, and the GRANDMA/Kilonova-Catcher (KNC) amateur program<sup>8</sup>. In addition to the photometric reports, a spectroscopic redshift measurement of GRB 241030A yields  $z = 1.411$  (Zheng et al. 2024; Li et al. 2024). Similarly (13:15:33 UT on 2024 October 30), we also conducted spectroscopic observations of GRB 241030A during 1h using the Gao-Mei-Gu (GMG) 2.4-meter telescope at Lijiang Observatory (Xin et al. 2020). The spectroscopic observations used the GMG grating–prism disperser #3, which provides a wavelength coverage of 3400–9100 Å (Wang et al. 2019), but we were not able to identify a clear signature allowing redshift determination.

## Appendix F: Observational data

<sup>8</sup> <http://kilonovacatcher.in2p3.fr/>

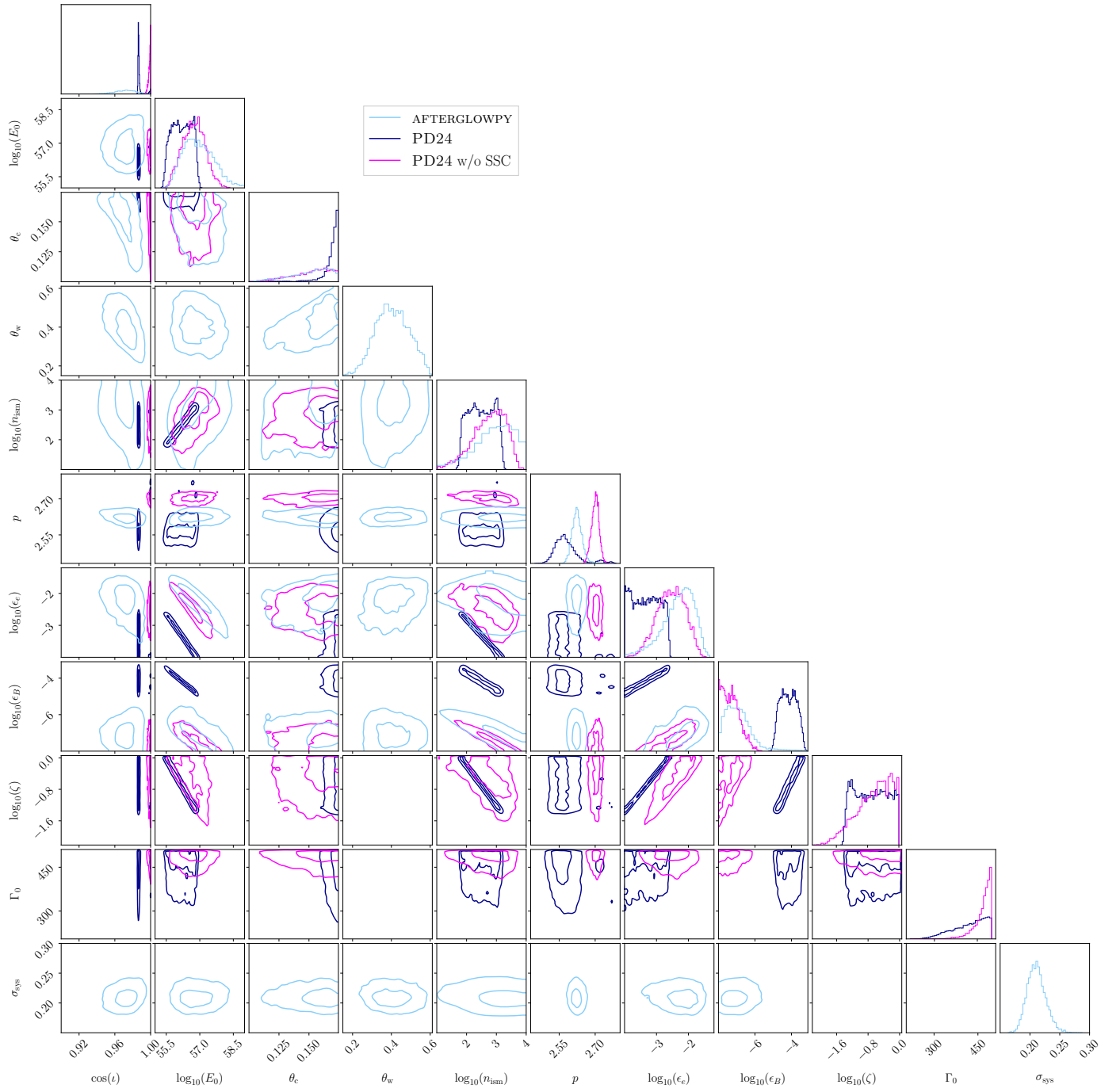


**Fig. D.1.** Posterior corner plot for the Bayesian analyses with the NMMA/AFTERGLOWPY gaussian jet model (light blue) and the PD24 model without SSC (pink) and with SSC (dark blue). Due to the different model parameters, certain columns and rows only show the posterior for either the NMMA/AFTERGLOWPY inference or the inference with PD24. The contours show the 39% and 86% credible regions.

**Table F.1.** Gamma/X-ray observations of GRB 241030A. Column (1) is the time delay between the observation and the GRB  $T_0$  in days. Column (3) is the unabsorbed flux density in Jy. Flux densities are computed at 2.77 keV for the *Swift*-XRT, *EP*-WXT and *EP*-FXT instruments, and at 1 GeV for *Fermi*-LAT. In Column (5), X indicates data points not used in the Bayesian light-curve analysis, while A and P denote data used in NMMA/AFTERGLOWPY or PD24, respectively.

$\Delta T$ (days)	MJD	Flux (Jy)	Instrument	Analysis
0.00116	60613.24286	$1.13 \pm 0.153 \times 10^{-3}$	Swift-XRT	X
0.00170	60613.243401	$1.07^{+1.28}_{-0.53} \times 10^{-10}$	Fermi-LAT	X
0.00194	60613.243645	$2.63 \pm 0.348 \times 10^{-3}$	Swift-XRT	X
0.00315	60613.244847	$1.02 \pm 0.169 \times 10^{-3}$	Swift-XRT	X
0.00403	60613.245727	$6.00^{+7.00}_{-2.86} \times 10^{-10}$	Fermi-LAT	X
0.00428	60613.245983	$1.88 \pm 0.257 \times 10^{-4}$	Swift-XRT	X
0.00555	60613.247253	$4.03^{+4.60}_{-1.87} \times 10^{-10}$	Fermi-LAT	P
0.00622	60613.247925	$3.77 \pm 0.575 \times 10^{-5}$	Swift-XRT	P
0.00766	60613.249357	$4.74^{+3.45}_{-1.73} \times 10^{-10}$	Fermi-LAT	P
0.00914	60613.250838	$2.28 \pm 0.375 \times 10^{-5}$	Swift-XRT	P
0.03142	60613.273125	$1.17 \pm 0.636 \times 10^{-5}$	EP-WXT	A-P
0.05687	60613.298567	$4.20 \pm 0.920 \times 10^{-6}$	Swift-XRT	A-P
0.12295	60613.364652	$2.16 \pm 0.478 \times 10^{-6}$	Swift-XRT	A-P
0.27378	60613.515478	$5.57 \pm 1.23 \times 10^{-7}$	Swift-XRT	A-P
0.45894	60613.700644	$2.47 \pm 0.563 \times 10^{-7}$	Swift-XRT	A-P
0.88551	60614.127212	$1.02 \pm 0.256 \times 10^{-7}$	Swift-XRT	A-P
0.90176	60614.143461	$6.66 \pm 0.653 \times 10^{-8}$	EP-FXT	A-P
2.55774	60615.799437	$1.70 \pm 0.321 \times 10^{-8}$	Swift-XRT	A-P
2.84056	60616.082257	$1.14 \pm 0.266 \times 10^{-8}$	EP-FXT	A-P
3.67543	60616.917135	$8.39 \pm 2.33 \times 10^{-9}$	Swift-XRT	A-P
4.45853	60617.700231	$5.53 \pm 1.31 \times 10^{-9}$	EP-FXT	A-P
6.38300	60619.624706	$3.72 \pm 1.15 \times 10^{-9}$	Swift-XRT	A-P
8.84158	60622.083285	$2.20 \pm 1.20 \times 10^{-9}$	Swift-XRT	A-P

**Table F.2.** UV/Optical observations of GRB 241030A. Column (1) is the time delay between the observation and the GRB  $T_0$  in days. Column (3) gives apparent magnitudes in the AB system, without any correction. In Column (6), a X means we did not use this data point for the Bayesian light curve analysis, an A or a P means this data point has been used for NMMA/AFTERGLOWPY or PD24, respectively.

$\Delta T$ (days)	MJD	Magnitude (AB)	Filter	Telescope	Analysis
(1)	(2)	(3)	(4)	(5)	(6)
0.00091	60613.24261	$16.24 \pm 0.27$	v	UVOT	X
0.00102	60613.242717	$16.21 \pm 0.04$	w	UVOT	X
0.00113	60613.242832	$16.15 \pm 0.03$	w	UVOT	X
0.00125	60613.242948	$16.04 \pm 0.03$	w	UVOT	X
0.00136	60613.243064	$15.65 \pm 0.09$	w	UVOT	X
0.00148	60613.243179	$15.65 \pm 0.09$	w	UVOT	X
0.00159	60613.243295	$15.71 \pm 0.08$	w	UVOT	X
0.00171	60613.243411	$15.55 \pm 0.09$	w	UVOT	X
0.00183	60613.243527	$15.89 \pm 0.02$	w	UVOT	X
0.00194	60613.243642	$15.97 \pm 0.02$	w	UVOT	X
0.00206	60613.243758	$16.25 \pm 0.04$	w	UVOT	X
0.00217	60613.243874	$16.45 \pm 0.04$	w	UVOT	X
0.00229	60613.24399	$16.61 \pm 0.05$	w	UVOT	X
0.0024	60613.244105	$16.68 \pm 0.05$	w	UVOT	X
0.00252	60613.244221	$16.64 \pm 0.05$	w	UVOT	X
0.00264	60613.244337	$16.49 \pm 0.04$	w	UVOT	X
0.00354	60613.245238	$14.42 \pm 0.03$	u	UVOT	X
0.00377	60613.245469	$14.08 \pm 0.03$	u	UVOT	X
0.004	60613.245701	$13.77 \pm 0.02$	u	UVOT	X
0.00423	60613.245932	$13.66 \pm 0.02$	u	UVOT	X
0.00446	60613.246164	$13.65 \pm 0.02$	u	UVOT	X
0.00469	60613.246395	$13.62 \pm 0.02$	u	UVOT	A-P
0.00493	60613.246627	$13.79 \pm 0.03$	u	UVOT	A-P
0.00516	60613.246858	$13.88 \pm 0.03$	u	UVOT	A-P
0.00539	60613.24709	$13.9 \pm 0.03$	u	UVOT	A-P
0.00562	60613.247321	$14.0 \pm 0.03$	u	UVOT	A-P
0.00585	60613.247553	$14.05 \pm 0.03$	u	UVOT	A-P
0.00608	60613.247784	$14.05 \pm 0.03$	u	UVOT	A-P
0.00631	60613.248016	$14.2 \pm 0.04$	u	UVOT	A-P
0.00649	60613.248188	$13.72 \pm 0.03$	b	UVOT	A-P
0.00669	60613.248388	$14.43 \pm 0.35$	w	UVOT	X
0.0068	60613.248504	$14.42 \pm 0.32$	w	UVOT	X
0.00692	60613.248619	$14.5 \pm 0.45$	w	UVOT	X

**Table F.3.** UV/Optical observations of GRB 241030A (continued from F.2)

$\Delta T$ (days)	MJD	Magnitude (AB)	Filter	Telescope	Analysis
(1)	(2)	(3)	(4)	(5)	(6)
0.00713	60613.24883	16.89 ± 0.11	uvw2	UVOT	X
0.00716	60613.24886	13.52 ± 0.06	v	UVOT	A-P
0.00751	60613.249207	13.66 ± 0.06	v	UVOT	A-P
0.00787	60613.249571	16.31 ± 0.1	uvm2	UVOT	X
0.00798	60613.249683	15.59 ± 0.06	uvw1	UVOT	X
0.00817	60613.249867	14.58 ± 0.04	u	UVOT	A-P
0.0084	60613.250099	14.52 ± 0.08	u	UVOT	A-P
0.00847	60613.250167	14.06 ± 0.04	b	UVOT	A-P
0.00865	60613.250355	14.82 ± 0.22	w	UVOT	X
0.00869	60613.250387	14.21 ± 0.08	b	UVOT	A-P
0.00877	60613.250471	14.84 ± 0.16	w	UVOT	X
0.00886	60613.250566	17.52 ± 0.25	uvw2	UVOT	X
0.00889	60613.250587	14.84 ± 0.21	w	UVOT	X
0.00921	60613.250913	17.43 ± 0.18	uvw2	UVOT	X
0.00924	60613.250943	14.04 ± 0.06	v	UVOT	A-P
0.00926	60613.250959	16.82 ± 0.23	uvm2	UVOT	X
0.00959	60613.25129	13.83 ± 0.09	v	UVOT	A-P
0.00972	60613.251419	16.15 ± 0.14	uvw1	UVOT	X
0.00995	60613.251654	16.6 ± 0.14	uvm2	UVOT	X
0.01007	60613.251766	15.86 ± 0.08	uvw1	UVOT	X
0.01859	60613.260289	14.96 ± 0.01	R	TRT-SRO	A-P
0.01945	60613.261148	15.05 ± 0.01	R	TRT-SRO	A-P
0.02029	60613.261996	15.08 ± 0.01	R	TRT-SRO	A-P
0.02316	60613.26486	15.29 ± 0.01	R	TRT-SRO	A-P
0.02485	60613.266556	15.4 ± 0.01	R	TRT-SRO	A-P
0.02653	60613.268234	15.47 ± 0.01	R	TRT-SRO	A-P
0.02822	60613.269922	15.56 ± 0.01	R	TRT-SRO	A-P
0.03309	60613.274792	15.72 ± 0.01	R	TRT-SRO	A-P
0.0356	60613.2773	15.8 ± 0.01	R	TRT-SRO	A-P
0.03809	60613.279796	15.88 ± 0.01	R	TRT-SRO	A-P
0.04061	60613.282308	15.96 ± 0.01	R	TRT-SRO	A-P
0.0431	60613.284797	16.0 ± 0.01	R	TRT-SRO	A-P
0.04558	60613.287284	16.08 ± 0.01	R	TRT-SRO	A-P
0.04809	60613.289789	16.15 ± 0.01	R	TRT-SRO	A-P
0.05095	60613.292653	16.21 ± 0.01	R	TRT-SRO	A-P

**Table F.4.** UV/Optical observations of GRB 241030A (continued from F.3)

$\Delta T$ (days)	MJD	Magnitude (AB)	Filter	Telescope	Analysis
(1)	(2)	(3)	(4)	(5)	(6)
0.05389	60613.295587	16.42 ± 0.05	r'	COLIBRÍ	A-P
0.05451	60613.296211	16.31 ± 0.01	R	TRT-SRO	A-P
0.05805	60613.299752	16.36 ± 0.02	R	TRT-SRO	A-P
0.06161	60613.303312	16.42 ± 0.01	R	TRT-SRO	A-P
0.06829	60613.309987	16.56 ± 0.02	R	TRT-SRO	A-P
0.07496	60613.316663	16.67 ± 0.02	R	TRT-SRO	A-P
0.0776	60613.319305	16.73 ± 0.05	r'	COLIBRÍ	A-P
0.08109	60613.322792	16.79 ± 0.05	r'	COLIBRÍ	A-P
0.08457	60613.326273	16.83 ± 0.05	r'	COLIBRÍ	A-P
0.08472	60613.326419	16.81 ± 0.02	R	TRT-SRO	A-P
0.08819	60613.329893	16.9 ± 0.05	r'	COLIBRÍ	A-P
0.09139	60613.33309	16.89 ± 0.02	R	TRT-SRO	A-P
0.09205	60613.333755	16.96 ± 0.05	r'	COLIBRÍ	A-P
0.09585	60613.337554	16.98 ± 0.05	r'	COLIBRÍ	A-P
0.09809	60613.33979	17.02 ± 0.02	R	TRT-SRO	A-P
0.09978	60613.34148	17.06 ± 0.05	r'	COLIBRÍ	A-P
0.10372	60613.345418	17.13 ± 0.05	r'	COLIBRÍ	A-P
0.10478	60613.346482	17.09 ± 0.02	R	TRT-SRO	A-P
0.10716	60613.348864	17.18 ± 0.05	r'	COLIBRÍ	A-P
0.11147	60613.35317	17.16 ± 0.02	R	TRT-SRO	A-P
0.11816	60613.359859	17.3 ± 0.04	R	TRT-SRO	A-P
0.11915	60613.360847	18.14 ± 0.05	u	UVOT	A-P
0.12266	60613.364361	18.19 ± 0.05	u	UVOT	A-P
0.12482	60613.36652	17.35 ± 0.05	R	TRT-SRO	A-P
0.12617	60613.367876	18.28 ± 0.05	u	UVOT	A-P
0.12871	60613.370408	17.8 ± 0.08	b	UVOT	A-P
0.1315	60613.373205	17.9 ± 0.05	B	TRT-SRO	A-P
0.14236	60613.384065	17.71 ± 0.04	V	TRT-SRO	A-P
0.14601	60613.387715	17.59 ± 0.04	R	TRT-SRO	A-P
0.15327	60613.394973	17.16 ± 0.06	I	TRT-SRO	A-P
0.25098	60613.492679	20.25 ± 0.17	uvw1	UVOT	X
0.3166	60613.558303	19.5 ± 0.07	u	UVOT	A-P
0.32652	60613.568218	19.14 ± 0.09	b	UVOT	A-P
0.37101	60613.612708	18.49 ± 0.06	I	KNC	A-P
0.38187	60613.623569	21.61 ± 0.41	uvm2	UVOT	X

**Table F.5.** UV/Optical observations of GRB 241030A (continued from F.4)

$\Delta T$	MJD	Magnitude	Filter	Telescope	Analysis
(days)		(AB)			
(1)	(2)	(3)	(4)	(5)	(6)
0.38192	60613.623623	18.92 ± 0.04	R	AbAO-T70	A-P
0.39121	60613.632913	20.74 ± 0.15	uvw1	UVOT	X
0.4485	60613.690206	20.14 ± 0.11	u	UVOT	A-P
0.45857	60613.700272	20.13 ± 0.19	b	UVOT	A-P
0.4998	60613.741503	19.06 ± 0.08	r'	KAO	A-P
0.50522	60613.746921	18.94 ± 0.05	i'	KAO	A-P
0.51064	60613.752342	18.75 ± 0.04	z'	KAO	A-P
0.52452	60613.766222	21.04 ± 0.18	uvw1	UVOT	X
0.53737	60613.779069	19.65 ± 0.05	g'	KNC	A-P
0.55271	60613.794411	19.31 ± 0.07	r'	KNC	A-P
0.60878	60613.85048	19.68 ± 0.16	r'	KNC	A-P
0.6637	60613.905404	19.9 ± 0.05	g'	KNC	A-P
0.68166	60613.923361	19.75 ± 0.07	R	HAO	A-P
0.68487	60613.92657	19.47 ± 0.06	r'	KNC	A-P
0.70787	60613.949575	20.14 ± 0.07	g'	KNC	A-P
0.7271	60613.968801	20.27 ± 0.06	g'	HAO	A-P
0.72935	60613.97105	19.9 ± 0.1	g'	KAO	A-P
0.7322	60613.9739	19.6 ± 0.13	r'	KNC	A-P
0.74699	60613.988689	20.43 ± 0.2	r'	KAO	A-P
0.75972	60614.001423	19.9 ± 0.07	i'	KAO	A-P
0.77125	60614.012949	19.82 ± 0.08	g'	KNC	A-P
0.77282	60614.014519	20.36 ± 0.07	R	KNC	A-P
0.77584	60614.017546	21.55 ± 0.32	uvw1	UVOT	X
0.77628	60614.017986	19.76 ± 0.24	R	FR/CTAN	A-P
0.78616	60614.027859	20.65 ± 0.16	u	UVOT	A-P
0.79275	60614.034449	19.59 ± 0.14	z'	KAO	A-P
0.8157	60614.057401	20.0 ± 0.25	V	KNC	A-P
0.83943	60614.081134	19.95 ± 0.06	r'	COLIBRÍ	A-P
0.84117	60614.082875	20.47 ± 0.28	b	UVOT	A-P
0.85432	60614.096023	20.95 ± 0.3	B	TRT-SRO	A-P
0.87975	60614.121453	19.71 ± 0.13	V	TRT-SRO	A-P
0.90525	60614.146949	23.82 ± 2.11	uvw2	UVOT	X
0.91086	60614.152565	21.0 ± 2.94	v	UVOT	A-P
0.9498	60614.191502	19.99 ± 0.06	R	TRT-SRO	A-P
0.9643	60614.206005	19.67 ± 0.12	I	TRT-SRO	A-P

**Table F.6.** UV/Optical observations of GRB 241030A (continued from F.5)

$\Delta T$	MJD	Magnitude	Filter	Telescope	Analysis
(days)		(AB)			
(1)	(2)	(3)	(4)	(5)	(6)
0.96999	60614.211694	20.35 ± 0.31	b	UVOT	A-P
1.13104	60614.372737	20.47 ± 0.23	V	TRT-SRO	A-P
1.16712	60614.408819	22.26 ± 0.83	uvm2	UVOT	X
1.17731	60614.419011	23.63 ± 1.42	uvw1	UVOT	X
1.18869	60614.430387	20.62 ± 0.1	r'	COLIBRÍ	A-P
1.2294	60614.4711	20.45 ± 0.06	r'	COLIBRÍ	A-P
1.22986	60614.471558	21.04 ± 0.48	u	UVOT	A-P
1.23027	60614.471968	20.66 ± 0.29	r'	COLIBRÍ	A-P
1.23271	60614.474416	20.4 ± 0.22	R	TRT-SRO	A-P
1.24359	60614.485294	19.7 ± 0.19	I	TRT-SRO	A-P
1.2545	60614.496205	20.7 ± 0.2	B	TRT-SRO	A-P
1.25696	60614.49866	20.7 ± 0.1	r'	COLIBRÍ	A-P
1.40663	60614.648327	20.0 ± 0.1	i'	TNOT	A-P
1.52624	60614.767941	20.34 ± 0.06	i'	AbAO-T150	X
1.52714	60614.768844	20.63 ± 0.05	r'	AbAO-T150	X
1.65471	60614.896412	20.8 ± 0.1	i'	KAO	A-P
1.67051	60614.912209	20.99 ± 0.19	R	HAO	A-P
1.6857	60614.927398	21.5 ± 0.1	g'	KAO	A-P
1.72339	60614.965087	20.7 ± 0.16	r'	KAO	A-P
1.86734	60615.109039	21.52 ± 0.2	r'	COLIBRÍ	A-P
2.18275	60615.424456	20.57 ± 0.04	r'	TNOT	A-P
2.49951	60615.741216	21.6 ± 0.2	i'	KAO	A-P
2.52714	60615.768394	21.83 ± 0.1	r'	AbAO-T150	X
2.57294	60615.814643	21.43 ± 0.11	r'	KAO	A-P
7.84252	60621.084225	22.62 ± 0.15	R	NAO-2m	A-P
8.46644	60621.708137	23.86 ± 0.28	R	NAO-1.5m	A-P